

**Texas A&M University
Mechanical Engineering Department
Turbomachinery Laboratory
Tribology Group**

**MEASUREMENTS OF ROTORDYNAMIC RESPONSE IN A
HIGH TEMPERATURE ROTOR SUPPORTED ON TWO
METAL MESH FOIL BEARINGS**

Research Progress Report to the TAMU Turbomachinery Research Consortium

TRC-BC001-2012

by

Luis San Andrés

Mast-Childs Tribology Professor
Principal Investigator

Thomas Abraham Chirathadam

Research Assistant

May 2012

METAL MESH FOIL BEARINGS: OPERATION AT HIGH TEMPERATURES

TRC Project, TEES # 32513/1519 FB

EXECUTIVE SUMMARY

MEASUREMENTS OF ROTORDYNAMIC RESPONSE IN A HIGH TEMPERATURE ROTOR SUPPORTED ON TWO METAL MESH FOIL BEARINGS

LUIS SAN ANDRES & THOMAS CHIRATHADAM, MAY 2012

Gas bearings in microturbomachinery (MTM) for power generation and also in automotive turbochargers must demonstrate adequate thermal management without performance degradation while operating in harsh environments.

The report presents rotor surface temperatures and rotordynamic measurements of a rigid rotor supported on a pair of metal mesh foil bearings (MMFBs) constructed in the laboratory ($L=38.1$ mm, $D=36.6$ mm). In the tests, to a maximum rotor speed of 50 krpm, an electric cartridge heats the hollow rotor over several hours while a steady inlet air flow rate at ~ 160 L/min cools the bearings. In the tests with the heater set to a high temperature (max. 200 °C), the rotor and bearing OD temperatures increase by 70 °C and 25 °C, respectively. Most rotor dynamic responses do not show a marked difference for operation under cold (ambient temperature) or a hot rotor conditions.

A linear rotordynamics structural model with predicted MMFB force coefficients delivers rotor response amplitudes in agreement with the measured ones for operation with the rotor at ambient temperature. There are marked differences in the peak amplitudes when the rotor crosses its (rigid body) critical speeds; the test bearings show lesser damping than predictions otherwise indicate. Waterfalls of rotor motion show absence of subsynchronous whirl frequency motions; the rotor-bearing system is stable for all operating conditions.

The measurements demonstrate that MMFBs can survive operation with severe thermal gradients, radial and axial, and with little rotordynamic performance changes when the rotor is either cold or hot. The experimental results, accompanied by acceptable predictions of the bearings dynamic forced performance, promote further metal mesh foil bearings as an inexpensive reliable technology for MTM.

TABLE OF CONTENTS

MEASUREMENTS OF ROTORDYNAMIC RESPONSE IN A HIGH TEMPERATURE ROTOR SUPPORTED ON TWO METAL MESH FOIL BEARINGS

LUIS SAN ANDRES & THOMAS CHIRATHADAM, MAY 2012

	<u>page</u>
Executive Summary	ii
List of Tables	iv
List of Figures	iv
Significance of work	1
Statement of work and budget	1
Introduction	3
Test rig facility and metal mesh bearings	6
Measurements and predictions of rotor dynamic response at room temperature for various mass imbalances	10
Measurement of temperature on the rotor and bearings for increasing electric heater temperatures and various rotor speeds	17
Temperature measurements without rotor spinning	19
Temperature measurements with a spinning rotor	20
Rotordynamic measurements with rotor operating at increasing temperatures	28
Conclusions	38
Nomenclature	39
References	40
Appendix A. Manufacturing a metal mesh foil bearing	42
Appendix B. MMFB stiffness and damping coefficients for rotordynamic response predictions	48

LIST OF TABLES

No		<u>page</u>
1	Nominal dimensions and specifications for rotor and MMFBs	9
2	Test cases for various rotor speeds and heater set temperatures (T_s)	19
3	Measured bearing cartridges and rotor OD temperatures for increasing heater set temperatures (T_s)	29
B.1	Predicted synchronous speed stiffness and damping coefficients for metal mesh bearing on rotor drive end (DEB). Static load = 7.4 N	48
B.2	Predicted synchronous speed stiffness and damping coefficients for metal mesh bearing on rotor free end (FEB). Static load = 5.7 N	49

LIST OF FIGURES

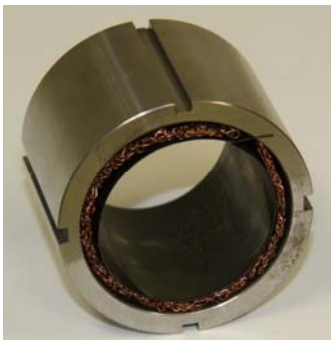
No		<u>page</u>
1	View of a metal mesh foil journal bearing (MMFB)	4
2	Exploded view of the MMFB assembly	5
3	Sectioned view of test rotor and bearings inside their housing.	6
4	Close-up view of rotor free end and cartridge heater	7
5	Metal mesh foil bearing with four compressed mesh pads	8
6	Finite element structural model of test rotor supported on MMFBs. A flexible coupling connects the drive motor to the connecting rod affixed to the rotor	11
7	Predicted damped natural frequency map for rotor-MMFB system. Insets show first two forward whirl mode shapes	12
8	Predicted damping ratios corresponding to natural frequencies in Fig. 7.	12
9	Normalized rotor response amplitude and phase angle versus shaft speed for out-of-phase imbalance masses: 240 mg and 360 mg. Measurements at rotor drive end horizontal direction during rotor ramp up (acceleration 600 rpm/s). Measurements show baseline subtraction	13
10	Measured and predicted rotor response amplitude and phase angle versus shaft speed for two out-of-phase imbalances (a) 240 mg and (b) 360 mg. Measurements at rotor drive end horizontal direction during rotor ramp up. Measurements show baseline subtraction	14
11	Measured and predicted rotor response amplitude and phase angle versus shaft speed for (a) in-phase and (b) out-of-phase 360 mg imbalance masses. Measurements at rotor free end vertical direction during rotor ramp up. Measurements show baseline subtraction	15

12	Waterfall plot of rotor response at its drive end, horizontal plane, out-of-phase imbalance masses=240 mg. Rotor acceleration 600 rpm/s.	16
13	Waterfall plot of rotor response at the rotor drive end, horizontal plane, out-of-phase imbalance masses=360 mg. Rotor acceleration 600 rpm/s.	16
14	Waterfall plot of rotor response at the rotor drive end, vertical plane, in-phase imbalance masses= 360 mg. Rotor acceleration 600 rpm/s.	17
15	Locations for measurement of temperatures on the rotor surface and bearing cartridges	18
16	No rotor spinning: Recorded test system component temperature rises versus elapsed time. Steady axial cooling flow into bearings at 160 L/min	21
17	Rotor spinning at 30 krpm: Recorded test system component temperature rises versus elapsed time. Steady axial cooling flow into bearings at 160 L/min	22
18	Rotor spinning at 40 krpm: Recorded test system component temperature rises versus elapsed time. Steady axial cooling flow into bearings at 160 L/min	23
19	Rotor spinning at 50 krpm: Recorded test system component temperature rises versus elapsed time. Steady axial cooling flow into bearings at 160 L/min	24
20	Equilibrium temperatures rise at rotor OD surface, free and drive ends, versus rotor speed. Steady axial cooling flow into bearings at 160 L/min	25
21	Rotor temperature rise relative to the duct temperature, $(T_{FE}-T_{duct})$ and $(T_{DE}-T_{duct})$, at equilibrium versus rotor speed. Steady axial cooling flow into bearings at 160 L/min.	26
22	Average bearing OD temperature rises (with std. deviation) versus rotor speed and increasing heater temperatures. Steady axial cooling flow into bearings at 160 L/min	27
23	Average bearing OD temperature rise with respect to duct temperature versus rotor speed and increasing heater temperatures. Steady axial cooling flow into bearings at 160 L/min	27
24	Rotor OD temperatures, free and drive ends, immediately before conducting a rotor speed ramp-up test. Steady axial cooling flow into bearings at 160 L/min. Data from tests with 240mg (out-of-phase) and 360 mg (in-phase) imbalances	29
25	Rotor synchronous response amplitude and phase versus shaft speed for out-of-phase imbalance masses = 240 mg. Measurements at rotor free end, (a) horizontal plane and (b) vertical plane. Rotor acceleration of 400 rpm/s. Cooling flow rate ~160 L/min.	31
26	Waterfall plot of rotor response at the rotor free end, horizontal plane, for out-of-phase imbalance masses = 240 mg. Rotor acceleration 400 rpm/s. Heater set temperature = 200 °C. Cooling flow rate ~160 L/min	32
27	Rotor synchronous response amplitude and phase versus shaft speed for out-of-phase imbalance masses = 240 mg. Measurements at rotor drive end (a) horizontal plane and (b) vertical plane. Rotor acceleration of 400 rpm/s. Cooling	33

	flow rate ~160 L/min.	
28	Rotor synchronous response amplitude and phase versus shaft speed for in-phase imbalance masses = 360 mg. Measurements at rotor free end (a) horizontal plane and (b) vertical plane. Rotor acceleration of 400 rpm/s. Cooling flow rate ~160 L/min.	34
29	Rotor synchronous response amplitude and phase versus shaft speed for in-phase imbalance masses = 360 mg. Measurements at rotor drive end (a) horizontal plane and (b) vertical plane. Rotor acceleration of 400 rpm/s. Cooling flow rate ~160 L/min.	35
30	Waterfall plot of rotor response at drive end, horizontal plane, with heater turned off (ambient temperature). Rotor acceleration 400 rpm/s. In-phase imbalance masses = 360 mg. Cooling flow rate ~160 L/min.	36
31	Waterfall plot the rotor response at the rotor drive end, vertical plane, for (a) heater turned off, and (b) heater set temperature = 200 °C. Rotor acceleration 400 rpm/s. In-phase imbalance masses = 360 mg. Cooling flow rate ~160 L/min.	37
A.1	Metal mesh foil bearing with four metal mesh pads	42
A.2	Bearing cartridge with a thin slot for affixing top foil. Inset shows the details of the thin slot	43
A.3	Top foil before assembly in a MMFB. The inner surface of the top foil coated with MoS ₂	44
A.4	Heat treatment of the top foil wrapped around a hot heater cartridge	45
A.5	Compressing metal mesh gauze into a flat strip in an ad-hoc die	46
A.6	Compressing flat metal mesh strip into arcuate mesh pads	47
B.1	Depiction of coordinate system for analysis. Eddy current sensors recording rotor displacement along <i>X</i> and <i>Y</i> directions. Static load applied along <i>Y</i> direction	48
B.2	Predicted synchronous speed stiffness and damping coefficients for metal mesh bearing on rotor drive end (DEB). Static load = 7.4 N	50

Significance of work

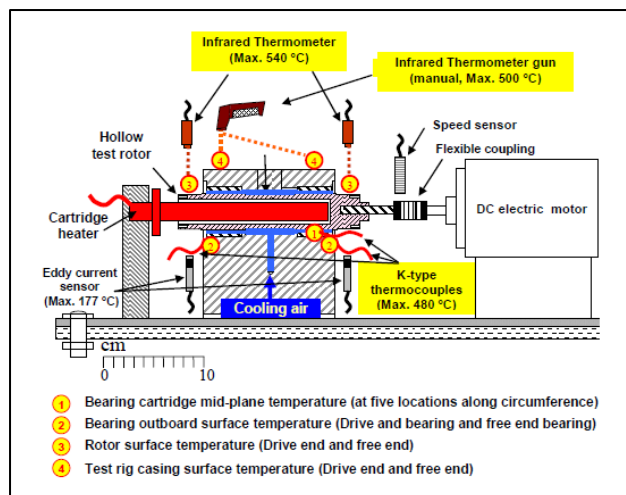
Oil-free microturbomachinery (MTM < 400 kW) seeks reliable and cost effective rotor-support bearing elements for commercially viable mass-production and widespread usage. Presently, compliant (foil type) gas bearings (bump foil, overleaf foils and multi-wound foils) are custom designed for particular applications and demand of excessive costs from design to manufacturing to prototype testing to field deployment. Industry demands of an inexpensive and reliable bearing technology that uses common materials and processes, is easy to scale, and proven to deliver adequate load support with stable stiffness and lots of damping.



Metal mesh foil bearing for oil-free turbomachinery

The Metal Mesh Foil Bearing (MMFB) is an alternative bearing type for supporting MTM. MMFBs are inexpensive by employing commonly available materials and a simple manufacturing process. In a MMFB, a ring shaped metal mesh provides a resilient support to a smooth top foil wrapped around a rotating journal; and a hydrodynamic film pressure builds up within the minute gap between the rotating journal and the top foil, thus providing a near frictionless load support. While mechanical energy dissipation (damping) in foil bearings is primarily due to Coulomb dry-friction, MMFBs offer much larger damping due to material hysteresis and dry-friction from the myriad of contacts within the metal mesh.

Statement of work and budget



The main objective of the proposed work is to demonstrate the reliable operation of MMFBs at elevated temperatures (max 200°C) and their ability to survive harsh environments with an adequate thermal management.

A high temperature rotor-bearing test rig constructed with NASA funds for evaluation of bump type foil bearings is available, see

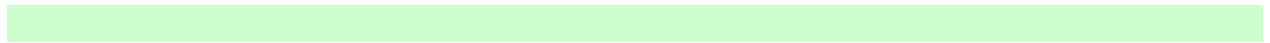
inset to the left. In the rig, an electric heater cartridge inside the hollow rotor warms the rotor to high temperature (max 300°C). The tasks for 2011/12 are:

- a) Construct two MMFBs fitting the existing bearing casing and shaft diameter, install the MMFBs in the test rig, align and balance the test rotor, and calibrate the high temperature instrumentation.
- b) Conduct experiments with rotor OD surface temperatures to 200°C and to a top rotor speed of 50 krpm. Measure bearing temperatures as the rotor (slowly) heats up and while providing increasing cooling streams. Assess the effectiveness of the cooling flow rates on managing the bearing and rotor temperatures. Rotor speed up and coast-down measurements will show rotor lift-off and touch down speeds, and the amplitude of motion data will serve to identify system damping ratios and effective bearing stiffnesses.

The TRC project was funded in December 2011 with the budget detail listed below. Supported by the PI incentive funds, Mr. Thomas Chirathadam, Ph.D. graduate student, conducted the work in 2011 and early 2012. Thomas is presently a research engineer at SwRI.

BUDGET FROM TRC FOR 2011-2012	Year I
Support for graduate student (20 h/week) x \$ 2,050 x 12 months	\$ 21,600
Fringe benefits (0.6%) and medical insurance (\$195/month)	\$ 2,488
Travel to (US) technical conference	\$ 1,200
Tuition three semesters (\$125 credit/hour x 24 credits in three semesters)	\$ 6,020
Supplies for test rig and construction of test bearings	<u>\$ 4,300</u>
Total Cost:	\$ 38,608

Mr. Joshua Norsworthy, a recent ME BS graduate and Research Assistant hired for the project, will continue to advance work by performing rotordynamic measurements to characterize foil bearings with shims and operating at high temperatures.



Introduction

Advanced micro-turbomachinery (MTM < 400 kW) requires cost-effective and reliable rotor support systems for efficient high speed operation at high temperature conditions, and in the presence of caustic process fluids [1, 2]. Automotive and aerospace applications require rugged gas bearings that are tolerant to misalignment and shock loads. Although conventional oil-lubricated bearings have a high load carrying capacity, large viscous drag losses at high rotor speeds and poor performance at high temperature [3] limit their use in specific applications. The burgeoning demand for hybrid/electric vehicles, auxiliary power units, high speed flywheel energy storage devices, and other systems that aim to reduce green house emissions and offering a low carbon foot print stimulates the growing interest in gas foil bearing technology.

Gas foil bearings (GFB) are traditionally used in MTM as they support high speed rotors on a thin film generated by the hydrodynamic viscous pumping of the ambient gas into the wedge shaped space between the spinning rotor and the bearing inner surface. Typically, a GFB consist of a smooth arcuate metal top foil and an elastic underspring support layer beneath it, both wrapped inside a solid cartridge. One end of the top foil is firmly affixed to the inner surface of the bearing cartridge.

GFBs offer other benefits such as reducing the number of components and system overall weight, avoiding altogether contaminated engine oil, and extending maintenance intervals. In addition to no restriction on DN life¹ and temperature limits typical for rolling element bearings, compliant surface bearings or GFBs also aid to increase efficiency by offering minimal drag power losses when operating airborne.

The metal mesh foil bearing (MMFB) [4] is a recent entrant in the GFB category with the promise of inexpensive manufacturing cost, large inherent material energy dissipation mechanism, and custom-tailored stiffness and damping properties enabling its ready scalability. Figure 1 depicts an isometric view of a MMFB and Figure 2 shows an exploded view of the bearing components. The bearing consists of a rigid steel cartridge with a compressed metal mesh pad and top foil wrapped inside. As the rotor spins within the MMFB, a thin gas film is generated that separates the surfaces in relative motion. The self-acting bearings, however, requires coatings on the top foil surface to reduce dry-sliding friction forces, and resulting drag torque and power loss, during start-up and shut-down processes. Ceramic powder or polymer

¹ DN = Diameter (D) in mm x rotational speed (N) in revolutions per minute

based foil coatings and chrome-plated shafts are commonly used in the industry for long service life performance [5]. The rotor operating speed, the structural stiffness of the support elastic structure in the bearing [6], and the applied coatings are the major factors affecting the load carrying capacity of a foil bearing.

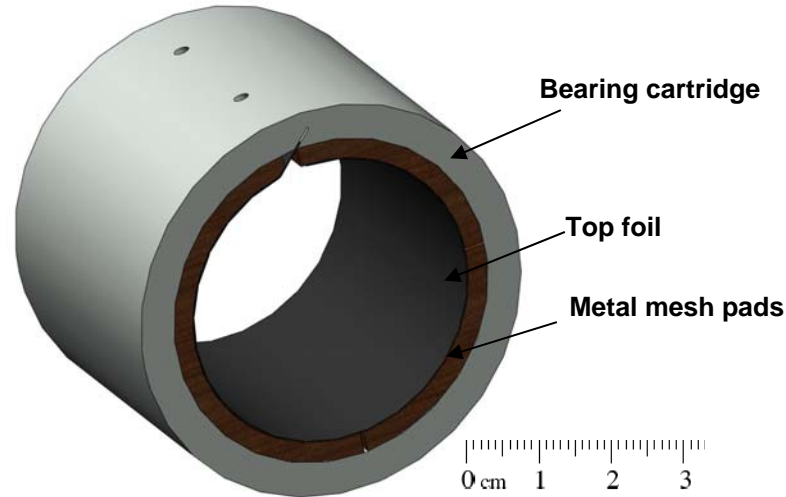


Fig. 1 View of a metal mesh foil journal bearing (MMFB).

Metal mesh, traditionally used as a vibration isolator [7] in gas turbine engines, operates satisfactorily in cryogenic temperatures as well as in high temperature environments [8]. Empirical design equations [9] render the structural force coefficients, stiffness (K) and equivalent viscous damping (C), of a metal mesh damper ring as nonlinear functions of the displacement amplitude, excitation frequency, and radial interference. The design equations [9], however, require of prior experimentation to determine an equivalent Young's modulus of the formed metal mesh ring.

San Andrés et al. [4] report constructing the first prototype of a MMFB ($L=D=28$ mm) with a metal mesh ring made of 0.3 mm Copper wire and compactness of 20 %. With the test bearing installed on a shaft with a slight preload, static load versus bearing deflection measurements display a cubic nonlinearity with large material hysteresis indicating significant mechanical energy dissipation. Identified structural stiffness and viscous damping coefficients decrease with increasing motion amplitudes, similarly as in metal mesh dampers [9]. On the other hand, with increasing excitation frequency, the bearing structural stiffness grows while the viscous damping coefficient rapidly decreases. A structural loss factor (material damping), not a viscous damping

type, best describes the mechanical energy dissipation of metal meshes. The experiments reveal a loss factor (γ) ~ 0.7 , higher than that in bump-type foil bearings, for example see Ref. [10]. In Ref. [4], the authors note that the metal mesh ring, with a large thickness of ~ 7 mm, undergoes significant sag or creep, resulting in the reduction of the magnitude of the structural force coefficients, upon operation and after multiple dismantling and re-assembly processes.

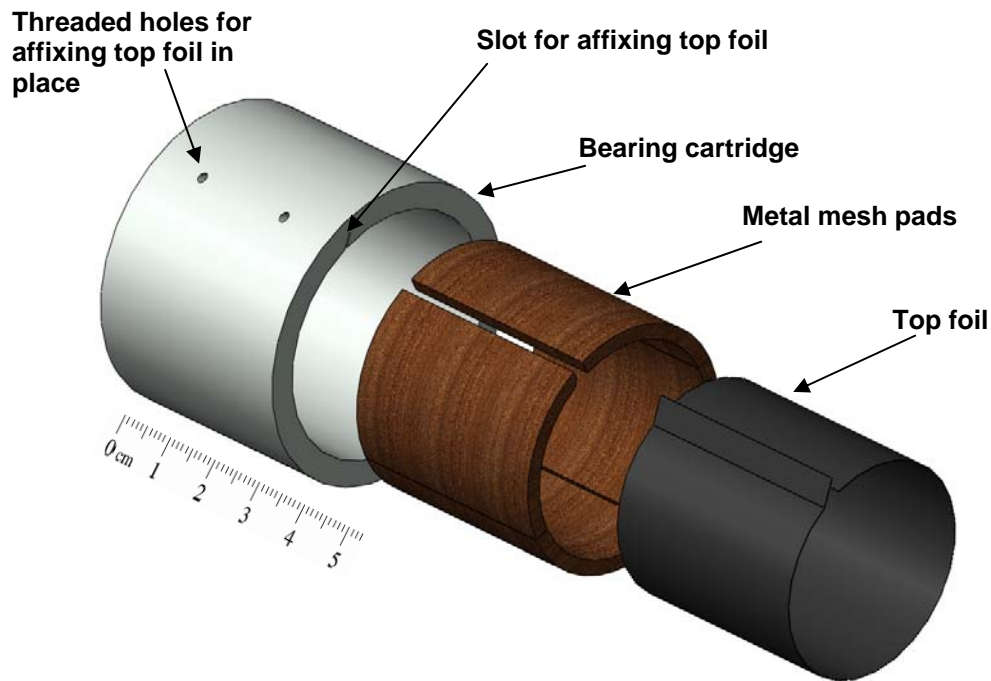


Fig. 2 Exploded view of the MMFB assembly.

San Andrés et al. [11] demonstrate the readiness of the novel bearing technology by measuring the MMFB break-away torque, rotor lift off and touchdown speeds during multiple start up and shutdown tests. Later, San Andrés et al. [12] extend the work reporting measured bearing load capacity and drag torque for rotor speeds up to 60 krpm. During airborne operation, i.e., with a gas film separating the rotating journal from the bearing, the friction coefficient is two orders of magnitude smaller than the dry-friction coefficient during operation at start up (and shut down) where dry-friction sliding is present.

The report presents measurements of rotordynamic response for a high temperature rigid rotor supported on two metal mesh foil bearings (MMFBs) and for operation with increasing mass imbalances. A finite element structural analysis models the rotor and with support connection to two metal mesh bearings modeled with an in-house predictive tool [13] to predict

the rotor synchronous response, amplitude and phase. An electric heater inside the hollow rotor heats the rotating system. The measurements of bearings and rotor temperatures for increasing heater temperatures reveal important features on the thermal energy management of the rotor-bearing system.

Test rig facility and metal mesh bearings

Figure 3 shows a sectioned 3D view of the test rig [13], with two metal mesh foil bearings supporting the rotor. The bearing span is ~103 mm. The test rig consists of a solid AISI 4140 steel block housing the test bearings, a high speed motor (max. 50 krpm) driving the rotor via a coupling, a cartridge heater, and instrumentation for recording rotor speed, rotor lateral displacements, and temperatures at various locations.

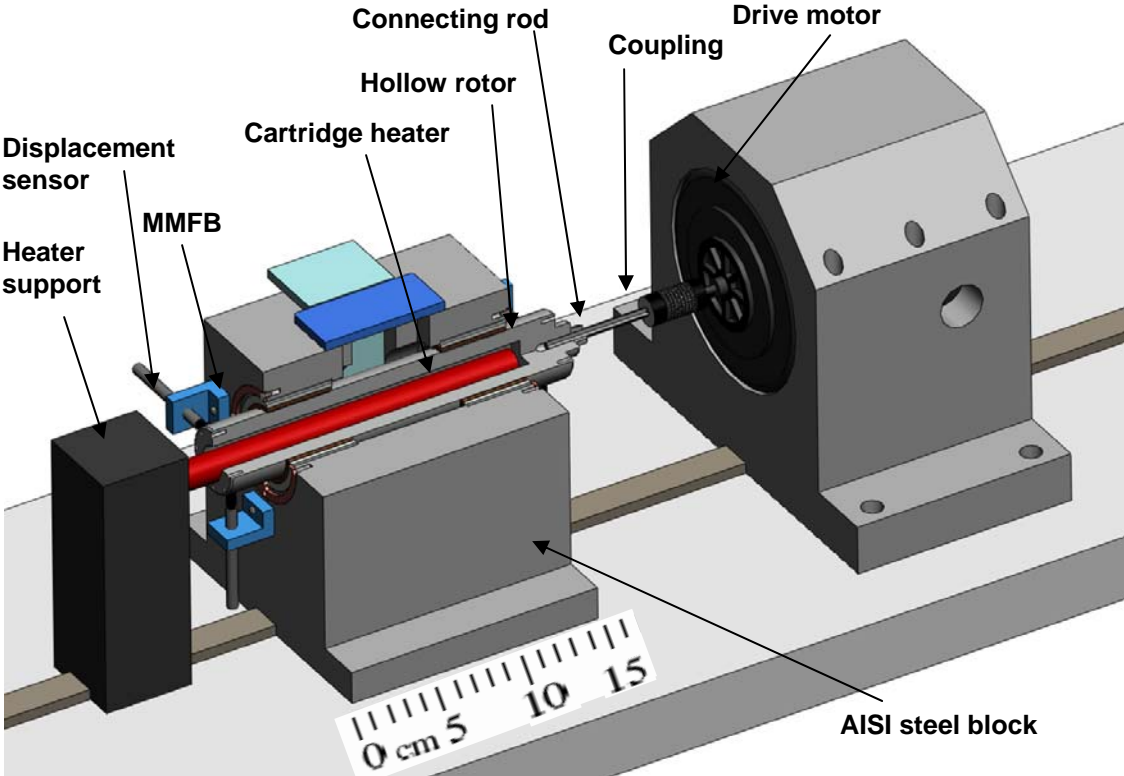


Fig.3 Sectioned view of test rotor and bearings inside their housing.

Dry high pressure air, from a shop compressor, is supplied to the enclosure (duct) inside the steel block at a set flow rate and which acts as a cooling flow to the test bearings. A thin ring

(end cap) tightly holds the bearings in place, as depicted in Figure 4. The end cap is ~ 2 mm thick and has an inner diameter slightly smaller than the bearing OD (50.8 mm).

A 15.9 mm diameter electric cartridge heater fits loosely inside the hollow rotor and heats the system² to a maximum temperature of 200° C. Two infrared thermometers (not shown in the figures) record the temperatures on the rotor surfaces near the bearings. See Ref. [13] for more details on high temperature measurements conducted in the test rig.

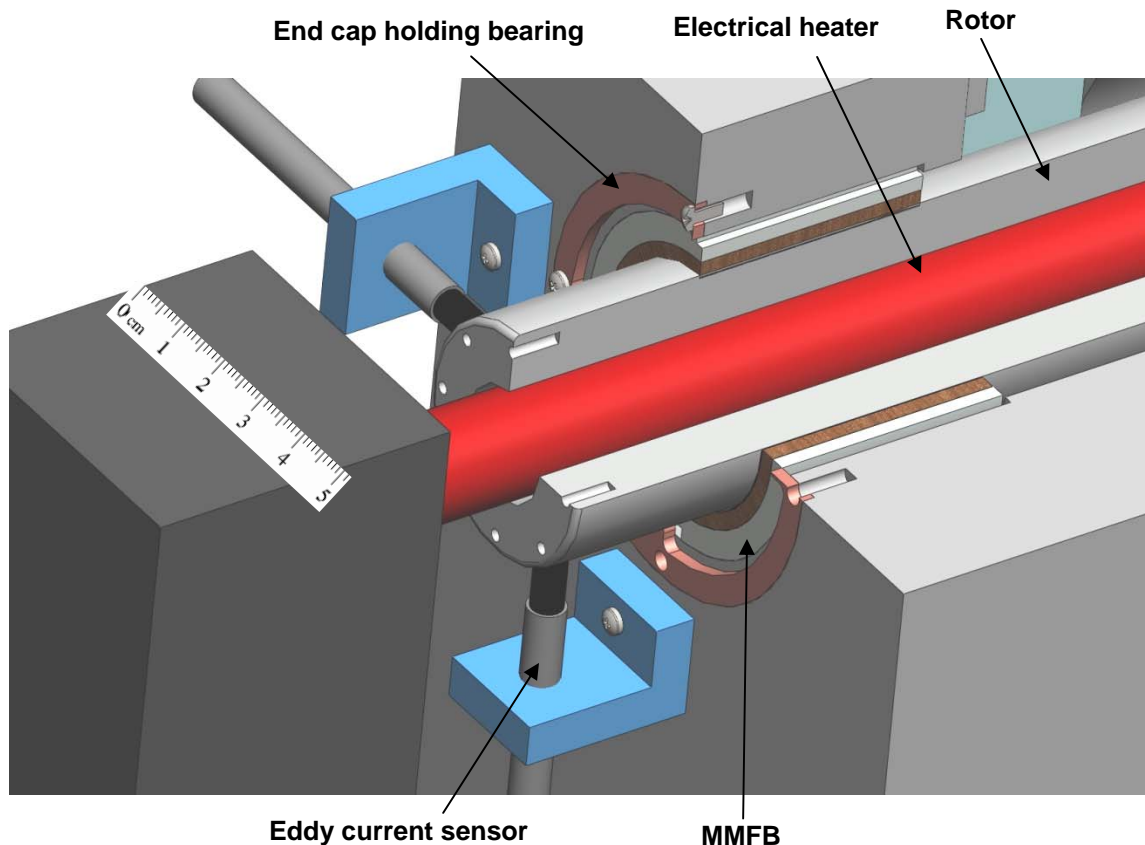


Fig. 4 Close-up view of rotor free end and cartridge heater.

Figure 5 shows a view of the test MMFB consisting of a stainless steel bearing cartridge, four compressed copper mesh pads³ ~2.6 mm thick, and a smooth pre-formed (hot rolled) alloy steel top foil, 0.120 mm in thickness. Appendix A describes in full the process to manufacture the metal mesh bearings. One end of the top foil slides to fit into a slot in the bearing cartridge. The metal mesh pads are manufactured by compressing weaves of thin copper wire into flat strips.

² A safety insulation shield, covering the entire test rig, is assembled during the high temperature measurements for operator safety.

³ Prior metal mesh foil bearings had a single ring shaped metal mesh pad [12]. However, for better dimensional control, the current bearings hold multiple arcuate pads.

The strips are later pressed under high pressure (~ 100 kN or higher) to curve them, and then inserted into the bearing cartridge. The top foil inner surface is spray coated with a thin layer ($< 10 \mu\text{m}$) of MoS_2 to reduce friction between the journal and top foil surface during rotor start-up and shut-down.

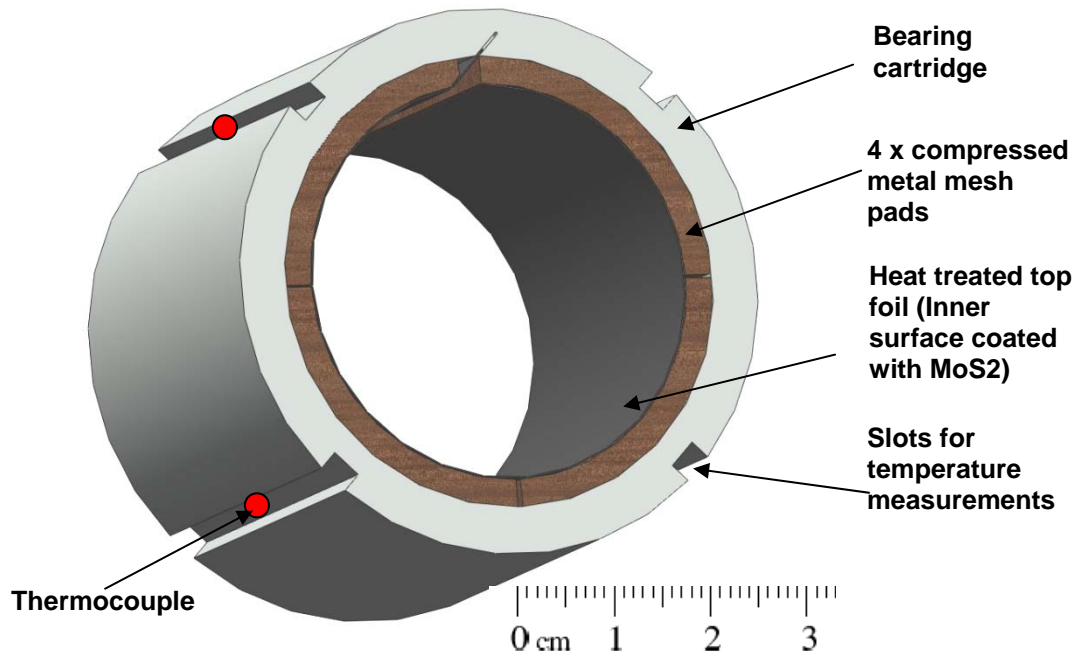


Fig. 5 Metal mesh foil bearing with four compressed mesh pads.

Table 1 lists the dimensions and specifications for the test bearing and rotor. As seen in Figure 5, four axial slots 90° apart, of depth 2mm and width 3mm, are machined on the OD the bearing cartridge. K type thermocouples cold-welded to the slots measure the cartridge OD temperature at its axial mid-span.

The hollow Inconel rotor⁴ is 200.66 mm long and weighs 1.360 kg (13.33 N), its outer diameter (D_o) = 36.51 mm and inner diameter (D_i) = 17.9 mm. At the rotor end face, eight equally spaced threaded holes, 13 mm deep, and at a radius of 15.5 mm permit the addition of imbalance masses. As the rotor center of mass⁵ (excluding the connecting rod) is located 105.8 mm from the rotor free end, the bearings carry unequal fractions of the rotor weight; with 7.39 N

⁴ Donated by Korea Institute of Science and Technology (KIST).

⁵ The c.g. of the combined rotor and the connecting rod is located 133.0 mm from the rotor free end, and applies 0.91 kg and 0.50 kg load at the rotor drive and free end bearings respectively.

($W/LD= 5.3$ kPa) on the bearing on the drive end (DE) side, and 5.94 N ($W/LD= 4.3$ kPa) on the bearing on the free end (FE) side of the rotor.

Table 1. Nominal dimensions and specifications for rotor and MMFBs

Rotor	Inconel 718
Mass, M	1.36 kg
Length	200.66 mm
Inner diameter, D_i	17.90 mm
Outer diameter, D_o	36.51 mm
Rotor diameter at bearings	36.51 ± 0.01 mm
Bearing span	103 mm
Bearings	
Cartridge outer diameter	50.80 mm
Cartridge inner diameter	42.00 ± 0.02
Inner diameter, D	36.58 ± 0.02 mm
Axial length, L	38.10 mm
Copper mesh pad thickness	2.6 mm
mesh density (compactness)	30 %
Wire diameter (mm)	0.30
Number of metal mesh pads	4
Top foil thickness	0.12 mm
Top foil (Chrome Nickel steel alloy)	Hardness Rockwell (40/45)
Radial clearance based on geometry	0.035 mm

Measurements and predictions of rotor dynamic response at room temperature for various mass imbalances

The rotordynamic measurements are conducted at room temperature (~ 22 °C) and with an air flow rate into the bearings maintained at ~ 160 L/min and with a supply gauge pressure of 1.9 bar (27.6 psig). The rotor response is recorded on the outboard of both bearings, along the horizontal and vertical directions. Inserted in the holes at the two end planes of the rotor, in-phase (0°) and out-of-phase (180°) imbalance masses equaling to 240 mg correspond to imbalance off-center displacements (u) of $5.5 \mu\text{m}$ and $15 \mu\text{m}$, respectively. Similarly, in-phase and out-of-phase imbalance masses of 360 mg give imbalance displacements (u)⁶ of $8.2 \mu\text{m}$ and $22.6 \mu\text{m}$, respectively. During the tests, the rotor accelerates at 600 rpm/s up to the highest rotor speed of 50 krpm (833 Hz) and then coasts down to rest. The motor does not actively control the rotor speed during the coast down process.

The remnant imbalance in the rotor, even after trim balancing in place, affects the rotor response. Hence, baseline response vectors are recorded and subtracted from the imbalance response vectors. Note that the DAQ system does not record the baseline response and imbalance response at identical rotor speeds, and most often, the number of vector elements is not equal either. A Mathcad ® program generates a re-sampled baseline response vector with elements equal to that of the measured imbalance response vector.

A linear finite element structural rotordynamic analysis (XLTRC² ®) predicts the response amplitude and phase of the rotor supported on the two MMFBs. Appendix B shows the predicted bearing force coefficients (synchronous speed) obtained with a recently developed computational model for metal mesh bearings [13].

Figure 6 depicts the finite element structural model of the test rotor and connecting rod, the added inertia and mass of the flexible coupling and the axial locations of the MMFBs. The imbalance masses are added at station 5 (rotor drive end) and station 16 (rotor free end) at a radius (r) equal to 15.5 mm.

⁶ In-phase (0°) imbalance masses (m_e) cause a rotor off-center displacement $u = 2 \times r (m_e / M)$. The imbalance mass is located at a radial distance of $r = 15.5$ mm from the rotor axis, and $M = 1.36$ kg is the rotor mass. The couple imbalance due to 180° out-of-phase placed masses (m_e) produces a rotor end side off-centered displacement $u = 2 \times r \times (m_e l^2 / I_T)$, where l is half the rotor length and I_T is the rotor transverse moment of inertia. These formulas apply to a simple 1DOF model (cylindrical and conical motions) of the rotor-bearing system.

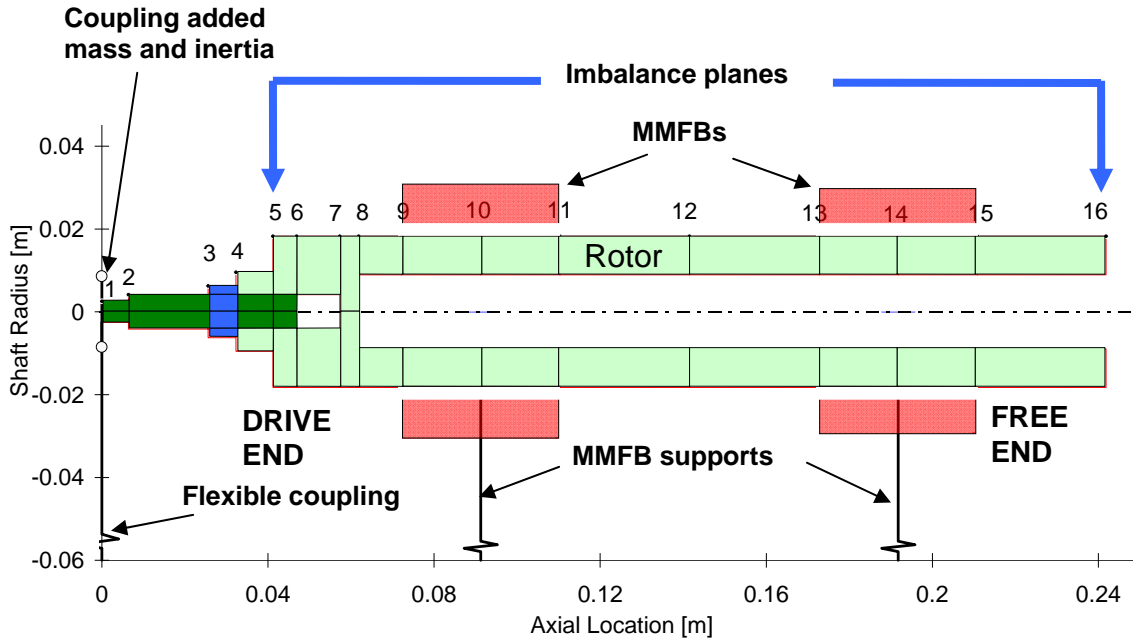


Fig. 6 Finite element structural model of test rotor supported on MMFBs. A flexible coupling connects the drive motor to the connecting rod affixed to the rotor

Figure 7 depicts the damped natural frequency map of the rotor bearing system for operation to 50 krpm, with insets showcasing two forward whirl mode shapes at 10 krpm. These mode shapes correspond to conical and \sim cylindrical rigid body modes at ~ 6.3 krpm and ~ 7.8 krpm. Figure 8 depicts the viscous damping ratios, corresponding to the two forward whirl modes, decreasing with rotor speed. This behavior is typical of a foil bearing since damping arises from dry-friction and/or mechanical hysteresis effects. It is well known that the equivalent viscous damping in a GFB is inversely proportional to whirl frequency (ω or rotor speed), i.e., $C \sim \gamma/\omega$, where γ is the bearing loss factor, a measure of the mechanical energy dissipation characteristic to the bearing. Note also that the damping ratio for the conical mode is nearly zero at the top rotor speeds (> 40 krpm) and likely to result in rotor motions with subsynchronous whirl frequencies.

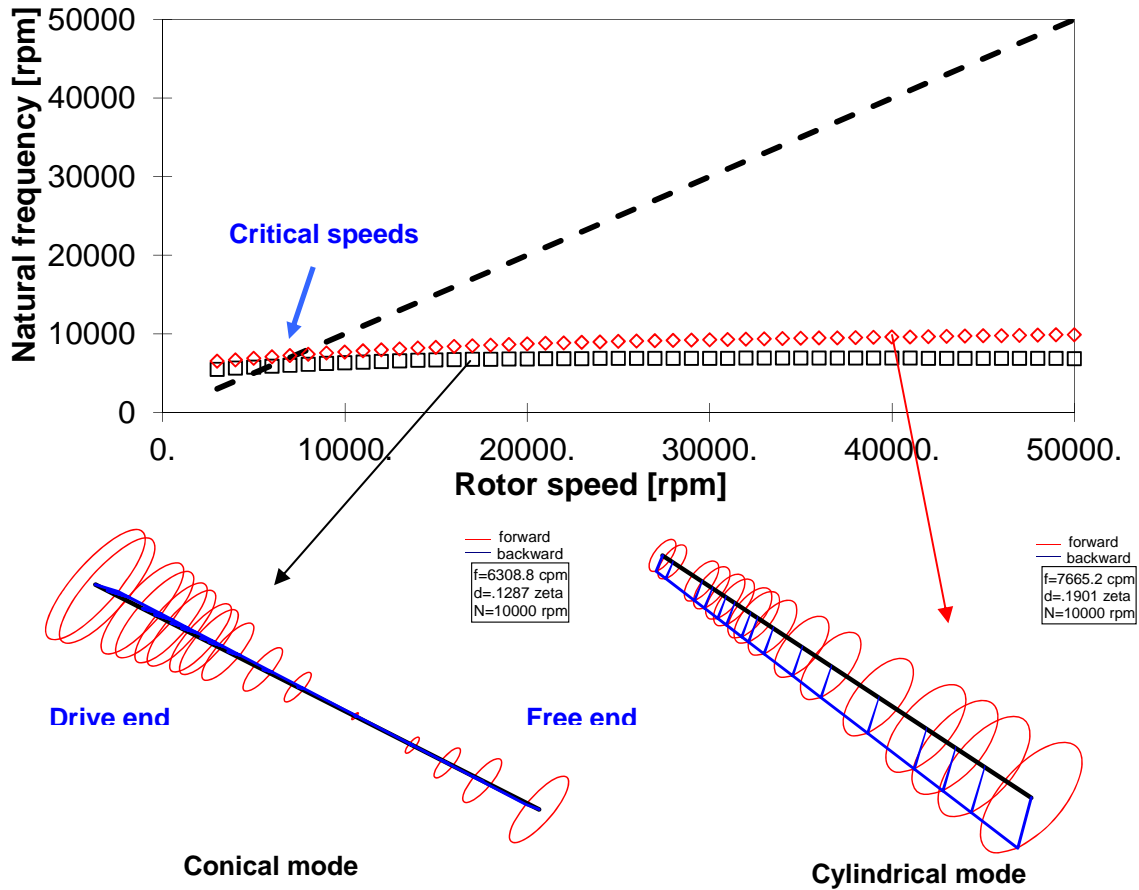


Fig. 7 Predicted damped natural frequency map for rotor-MMFB system. Insets show first two forward whirl mode shapes

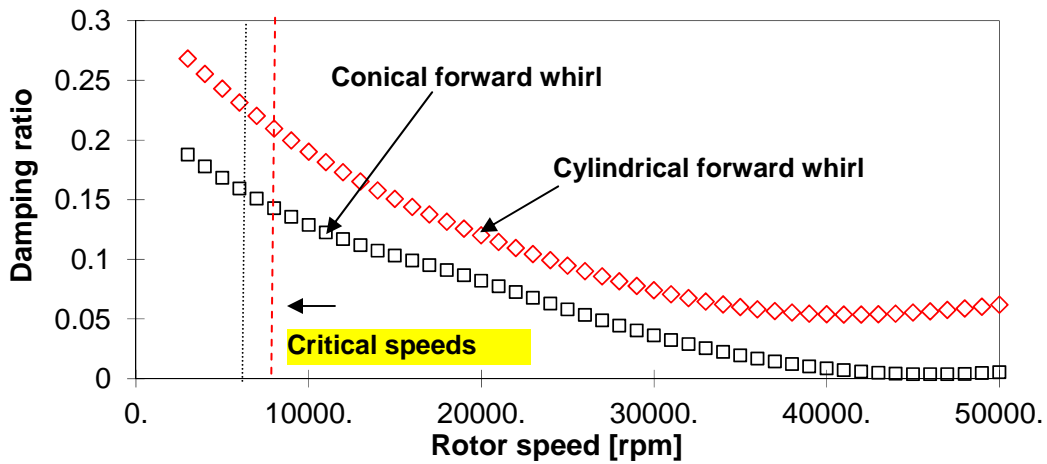


Fig. 8 Predicted damping ratios corresponding to natural frequencies in Fig. 7.

Figure 9 shows the normalized⁷ rotor response amplitude and phase angle measured at the rotor drive end, horizontal direction, for measurements with out-of-phase (180°) imbalance masses, 240 mg ($u = 15 \mu\text{m}$) and 360 mg ($u = 22.6 \mu\text{m}$). The normalized response amplitudes in the speed range from 10 krpm to 50 krpm show comparable magnitudes indicating that the system behaves linearly. At the critical speed, ~ 7 krpm, the peak normalized amplitude for the test with the largest imbalance (360 mg) is slightly larger than that for the 240 mg imbalance.

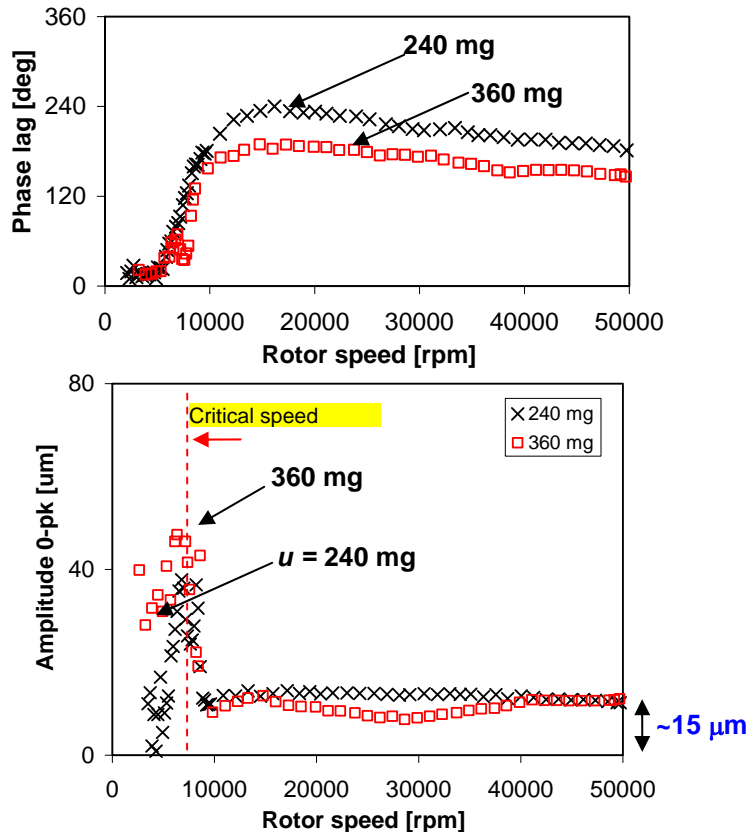


Fig. 9 Normalized rotor response amplitude and phase angle vs shaft speed for out-of-phase imbalance masses: 240 mg and 360 mg. Measurements at rotor drive end horizontal direction during rotor ramp up (acceleration 600 rpm/s). Measurements show baseline subtraction

Figure 10 shows the predicted and measured rotor response- angle of phase lag and displacement amplitude- at the rotor drive, horizontal direction, obtained for two out-of-phase (180°) imbalance masses, 240 mg ($u = 15 \mu\text{m}$) and 360 mg ($u = 22.6 \mu\text{m}$). At high speeds, the synchronous response amplitude for the larger imbalance mass (360 mg) is proportionately larger

⁷ The rotor response amplitude for $u = 22.6 \mu\text{m}$ ($m_e=360$ mg) is normalized by multiplying its amplitude times the ratio of smallest imbalance mass to the current imbalance mass.

than that with a 240 mg imbalance mass. The predictions, amplitude and phase, agree well with the measured displacements for the lowest imbalance (240 mg). However, for the larger mass of 360 mg, the measured peak response amplitude when traversing the critical speed is much larger than the prediction. The difference points out to the test MMFBs offering lesser damping than predicted.

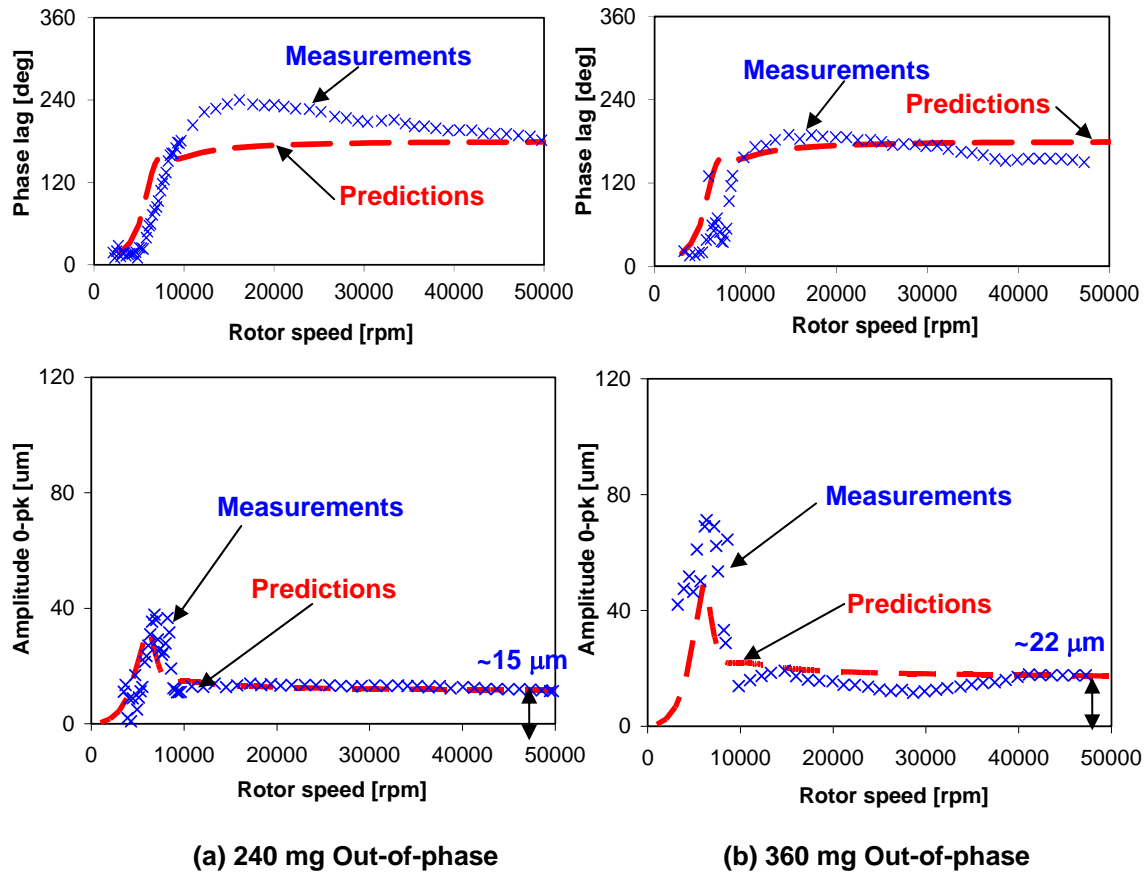


Fig. 10 Measured and predicted rotor response amplitude and phase angle versus shaft speed for two out-of-phase imbalance masses (a) 240 mg and (b) 360 mg. Measurements at rotor drive end horizontal direction during rotor ramp up. Measurements show baseline subtraction

Figure 11 shows the predicted and measured rotor response, phase angle and amplitude, at the rotor free end, vertical direction, for (a) in-phase and (b) out-phase imbalance masses $m_e=360$ mg, corresponding to imbalance displacements of $u = 8.2 \mu\text{m}$ and $22.6 \mu\text{m}$, respectively.

The measurements show the effect of adding the same imbalance masses, first in-phase and next out-of-phase at the end planes. The predicted and measured peak response amplitudes are comparable. While the finite element model under-predicts the response amplitudes for the tests

with out-of-phase imbalance mass of 360 mg, the predictions and measurements agree well for the in-phase imbalance of 360 mg.

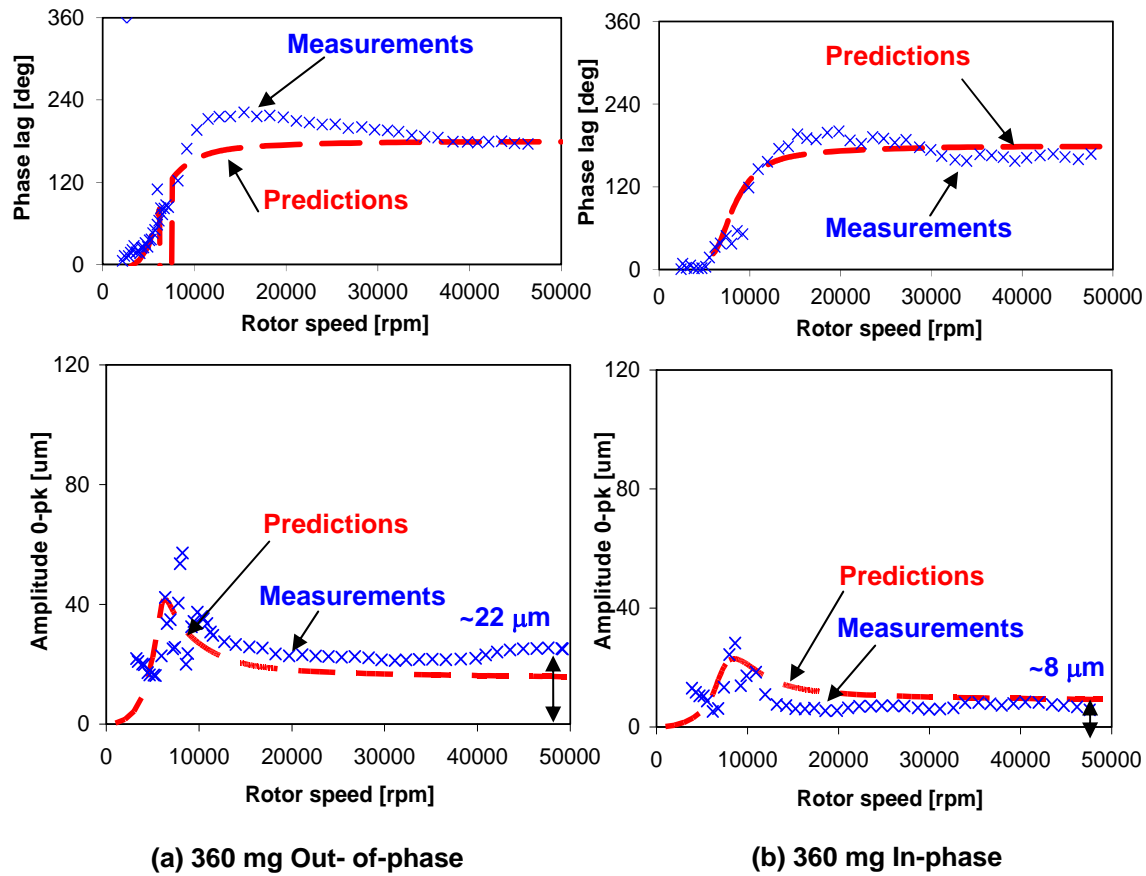


Fig. 11 Measured and predicted rotor response amplitude and phase angle versus shaft speed for (a) In-phase and (b) out-of-phase 360 mg imbalance masses. Measurements at rotor free end vertical direction during rotor ramp up. Measurements show baseline subtraction

Figures 12 and 13 show waterfall plots of the recorded rotor responses at the rotor drive end (horizontal plane), for out-of-phase imbalance masses equaling 240 mg and 360 mg, respectively. The rotor acceleration is 600 rpm/s (10 Hz/s). The plots show large amplitudes of synchronous motion (1X) as the rotor traverses a critical speed. 2X and 3X vibration components are present, although are small in amplitude. No sub-synchronous whirl motions appear in the measurements even at the highest rotor speed (50 krpm), in spite of the little to null viscous damping in the bearings.

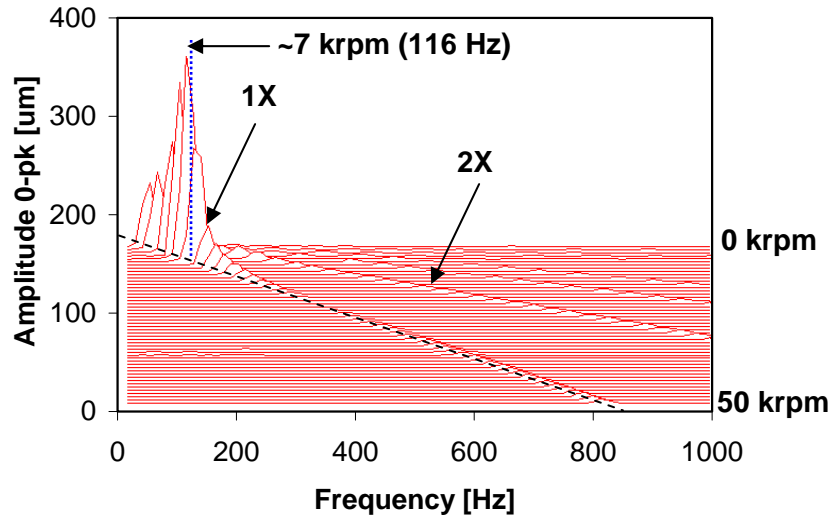


Fig. 12 Waterfall plot of rotor response at its drive end, horizontal plane, for out-of-phase imbalance mass of 240 mg. Rotor acceleration 600 rpm/s.

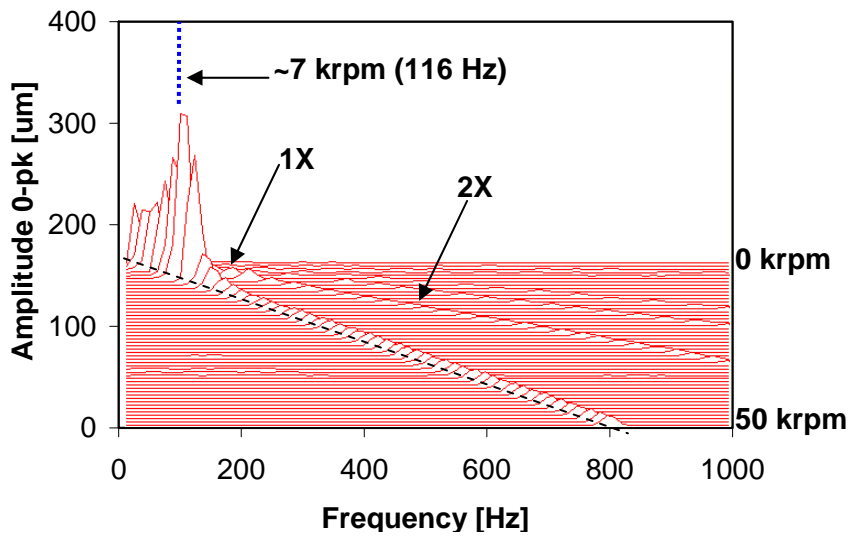


Fig. 13 Waterfall plot of rotor response at the rotor drive end, horizontal plane, for out-of-phase imbalance mass of 360 mg. Rotor acceleration 600 rpm/s.

Figure 14 depicts the waterfall plot of rotor response at its free end, vertical plane, for an in-phase imbalance mass of 360 mg. Again, the response is clean without any anomalies.

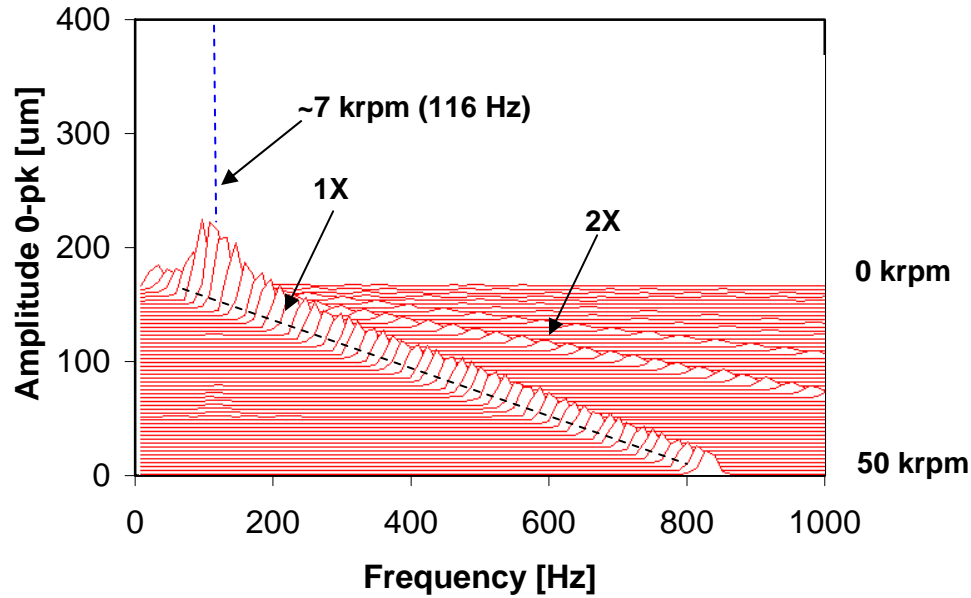


Fig. 14 Waterfall plot of rotor response at the rotor drive end, vertical plane, for in-phase imbalance mass of 360 mg. Rotor acceleration 600 rpm/s.

Measurement of temperature on the rotor and bearings for increasing electric heater temperatures and various rotor speeds

The evaluation of performance for MMFBs operating at high temperatures, especially during extended times, is required before MMFBs can be implemented into power generation micro-turbomachinery. This section presents (i) rotor and bearing temperature measurements with the rotor at rest and spinning at 30 krpm, 40 krpm, and 50 krpm and (ii) the dynamic response of the rotor while accelerating from rest to a maximum speed of 36 krpm. In the tests, the heater set temperature (T_s) is fixed at 22 °C (room temperature), 100 °C, 150 °C, and 200 °C.

The bearing and rotor temperatures are measured at ten locations, as depicted in Figure 15. T_1 - T_4 and T_5 - T_8 denote K-type thermocouples recording the temperatures at the bearing cartridge OD near the rotor free and drive ends, respectively. Infrared thermometers record the rotor OD surface temperature at its free and drive ends, T_{FE} and T_{DE} , respectively. The cartridge heater heats the rotor non-uniformly along its length [14], with the rotor free end being substantially

hotter than the drive end. The cooling air flow rate into the test bearings is maintained steady at $\sim 160 \text{ L/min}$ ⁸ with an inlet upstream gauge pressure of 1.9 bar (27.6 psig) for all tests.

Note that, for tests with the heater turned off, although the ambient temperature is $\sim 22 \text{ }^\circ\text{C}$, upon operation, for rotor speeds from 30 krpm to 50 krpm, the rotor temperature rises to a stationary magnitude; varying from $\sim 32 \text{ }^\circ\text{C}$ to $38 \text{ }^\circ\text{C}$ at the rotor free end, and $\sim 28 \text{ }^\circ\text{C}$ to $33 \text{ }^\circ\text{C}$ at the rotor drive end. Also, with the rotor spinning at 30 krpm, 40 krpm, and 50 krpm, the process takes 20s, 35s, and 55s, respectively, to reach thermal equilibrium while the heater is turned off. Note that the viscous drag losses cause the temperature rise.

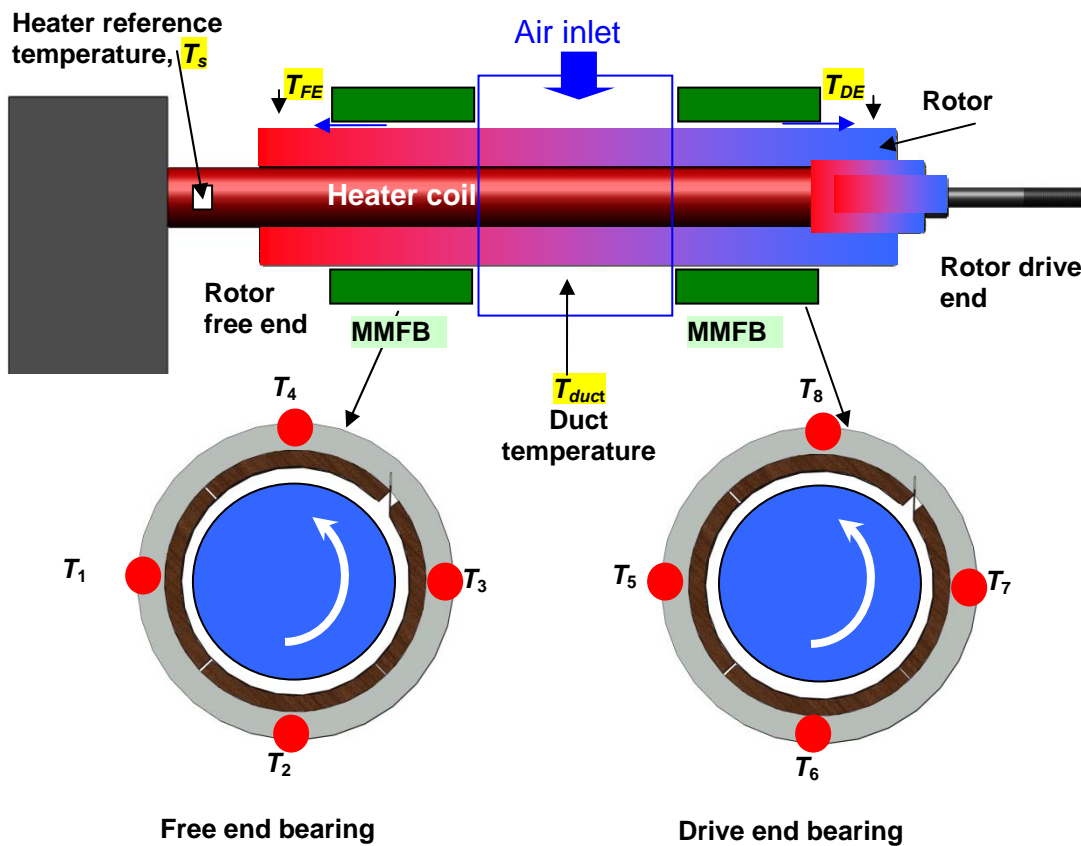


Fig. 15 Locations for measurement of temperatures on the rotor surface and bearing cartridges

⁸ In prior tests [15] with two similar bump type foil bearings supporting the rotor, a cooling flow rate of $\sim 160 \text{ L/min}$ was found to adequately cool the rotor and the two bearing during high temperature tests, and hence this flow rate is chosen for the current tests. The flowmeter is calibrated by the manufacturer at 1 atmosphere and 21°C . The uncertainty in the measured flow is $\pm 1.5\%$ of the full scale range (500 L/min).

Table 2 shows the various test cases representing increasing set temperatures for the heater ($T_s = \sim 22$ °C with heater off, 100 °C, 150 °C, and 200 °C) and for the rotor at rest and spinning at 30 krpm, 40 krpm, and 50 krpm. The rotor and bearing temperatures are recorded every five minutes until the system reaches thermal equilibrium⁹.

For test case #1, the rotor is at rest and the heater set temperature is increased, in steps of 50 °C, up to 200 °C, while recording the temperatures continuously until the system reaches equilibrium for each set temperature. For test cases #2-4, each at a constant rotor speed, the bearings and rotor temperatures are recorded until the system reaches equilibrium. The results show the temperature rise at each measuring location, i.e., the difference between the recorded temperature and the steady ambient temperature before commencement of the experiment.

Table 2. Test cases for various rotor speeds and heater set temperatures (T_s)

Test case #	Heater set Temperature, T_s [°C]	Rotor speed [krpm]	Time [min]
1	~ 22 (Heater off) $\rightarrow 100 \rightarrow 150 \rightarrow 200$	0	135
2	~ 22 (Heater off) $\rightarrow 100 \rightarrow 150 \rightarrow 200$	30	145
3	~ 22 (Heater off) $\rightarrow 100 \rightarrow 150 \rightarrow 200$	40	150
4	~ 22 (Heater off) $\rightarrow 100 \rightarrow 150 \rightarrow 200$	50	230
			Overall : 11 hr

Temperature measurements without rotor spinning

Figure 16 depicts, for test case # 1 (no rotor spinning), the temperature rise of the rotor free (T_{FE}) and drive (T_{DE}) ends, the bearing sleeves (T_{1-4} and T_{5-8}), and the inlet¹⁰ duct (T_{duct}) versus elapsed time while the rotor remains at rest. These measurements are later used to derive the effect of rotor spinning on the temperature distribution in the bearings.

Since the electric heater heats non-uniformly the rotor along its axial length [13], the equilibrium temperatures at the rotor free and drive ends are dissimilar, with the rotor free end

⁹ If any temperature fluctuation is less than 1 °C within a 15 minute time period, the system is considered to be in thermal equilibrium.

¹⁰ The *duct* temperature is recorded inside the enclosure adjacent to the bearings. This temperature is not that of the cold supply air because the air stagnates at this location.

being hotter than the drive end. Note that the air flow cooling the coupling near the rotor drive end also cools the rotor drive end. With increasing heater set temperatures (up to 200 °C), the difference between the equilibrium temperatures at the rotor drive and free ends increases, resulting in a larger thermal gradient along the rotor axial length. The air temperature inside the enclosure (duct) of the steel block housing the bearings also increases with increasing heater set temperatures and follows a trend similar to that of the rotor surface temperatures.

T_1 to T_4 and T_5 to T_8 are the temperatures measured on the outer surface of the bearing cartridges – free and drive end- at their mid-span. The temperatures around the bearing cartridge circumference are not identical, varying by a maximum of 4 °C at the highest heater set temperature of 200 °C. While the rotor surface temperature reaches thermal equilibrium quickly, the bearing cartridge outer surfaces require considerably longer time (typically > 30 min). However, the rate of increase in temperature after ~ 20 min is rather small. Hence, when the bearing temperatures do not increase more than 1 °C in a 15 minute time interval, the system is considered to be in thermal equilibrium and the heater set temperature increased to the next magnitude. The rate of increase in the temperature of the bearing cartridge is considerably lesser than that for the rotor. The steady cooling air flow and the heat loss by conduction to the steel block removes heat from the bearing. Although the temperature rise at the rotor free end is much higher than that at the rotor drive end, the two bearing cartridge temperatures are nearly identical.

Temperature measurements with a spinning rotor

Figures 17, 18, and 19 depict the temperature rise on the rotor free end (T_{FE}) and drive end (T_{DE}), of the bearing sleeves (T_1 - T_8), and the duct air (T_{duct}) versus elapsed time while the rotor spins at 30 krpm, 40 krpm, and 50 krpm respectively. The cooling flow into both bearings is at a rate of ~ 160 L/min. The trends in the variation of the temperature rise of the components, in general, follow patterns similar to those without rotor spinning. However, while spinning at 30 krpm - 50 krpm, even without the heater turned on, the temperatures on the rotor and the bearings slightly increase.

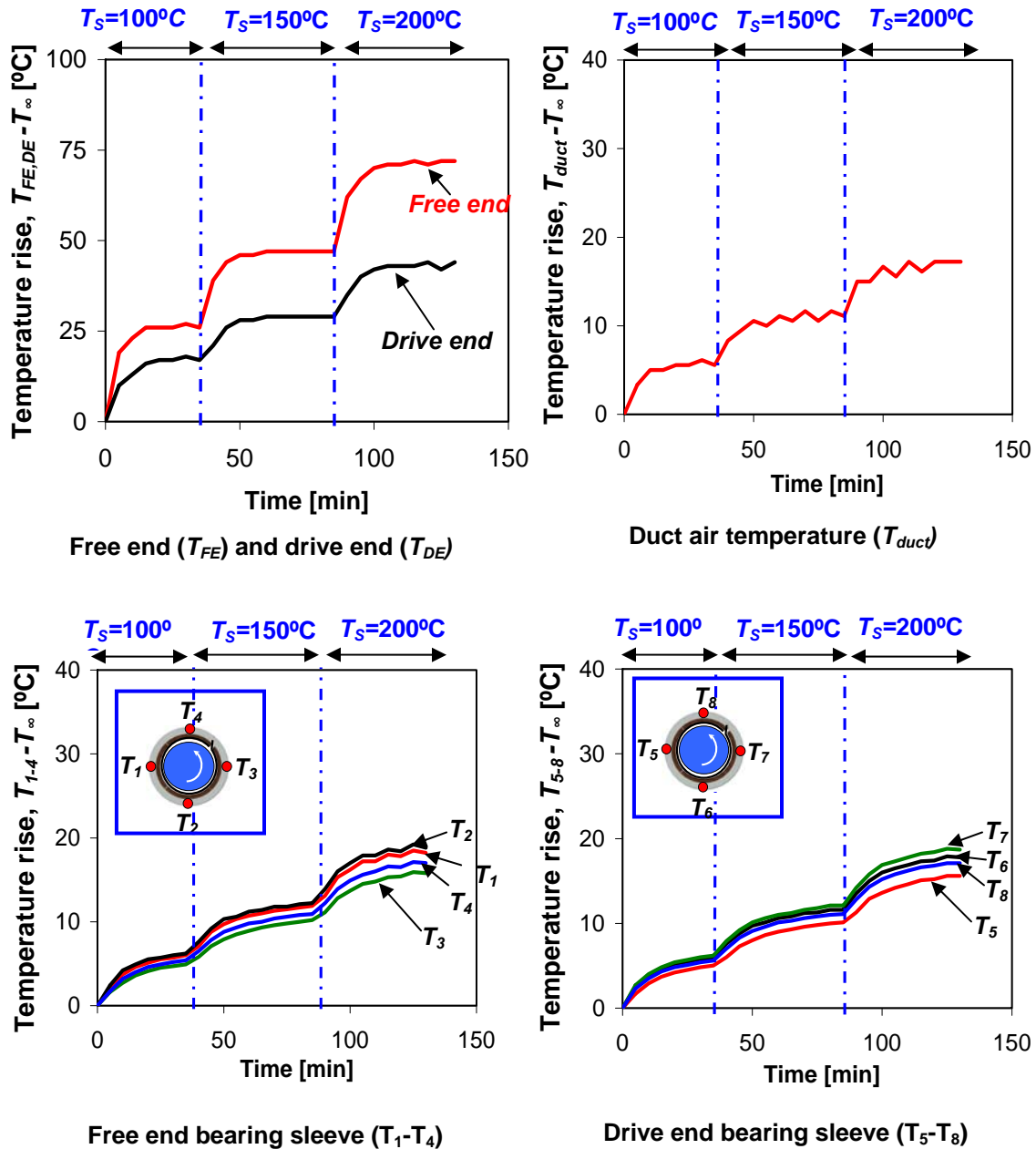
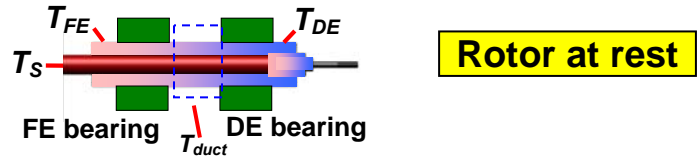


Fig. 16 **No rotor spinning**: Recorded test system component temperature rises versus elapsed time. Steady axial cooling flow into bearings at 160 L/min

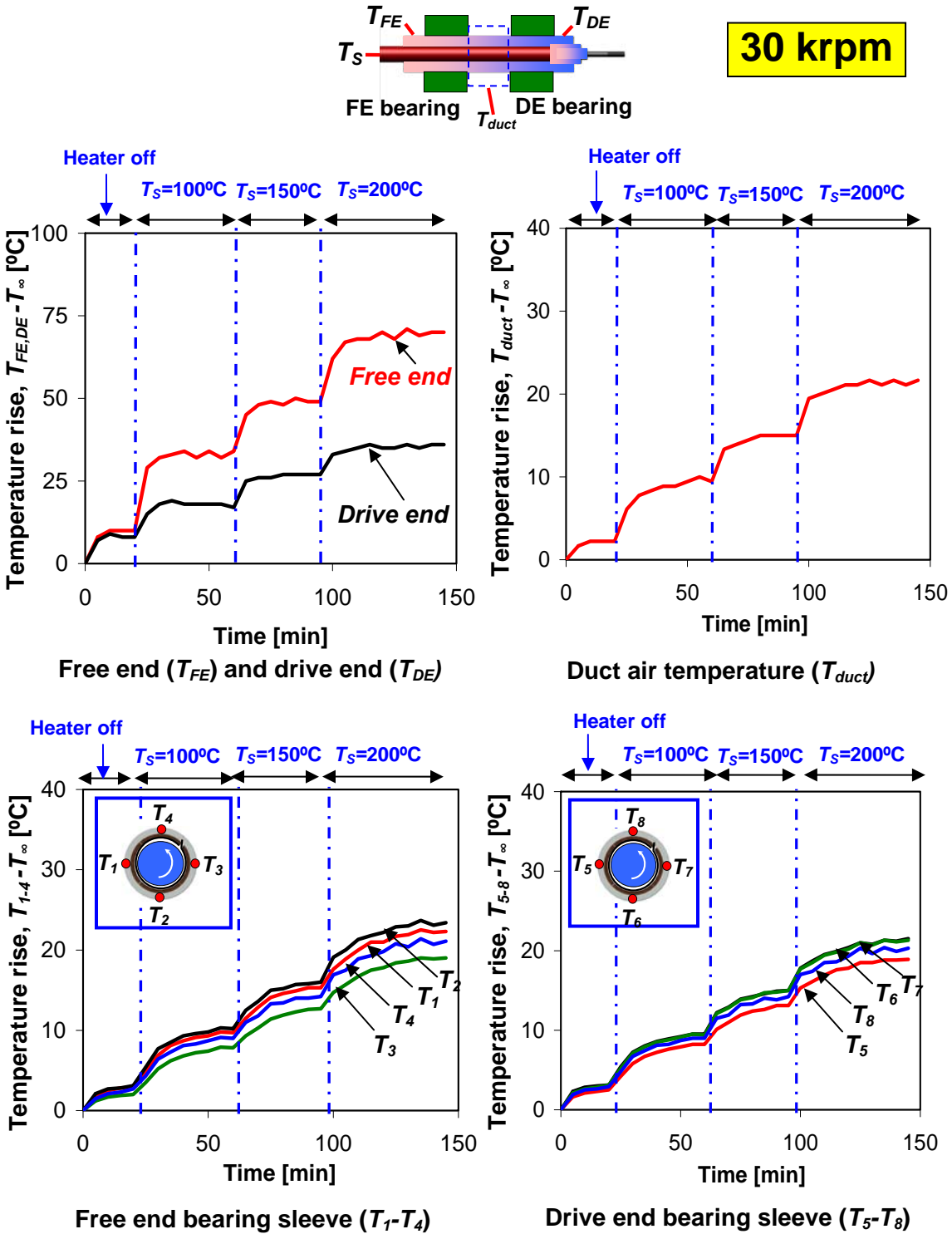


Fig. 17 Rotor spinning at 30 krpm: Recorded test system component temperature rises versus elapsed time. Steady axial cooling flow into bearings at 160 L/min

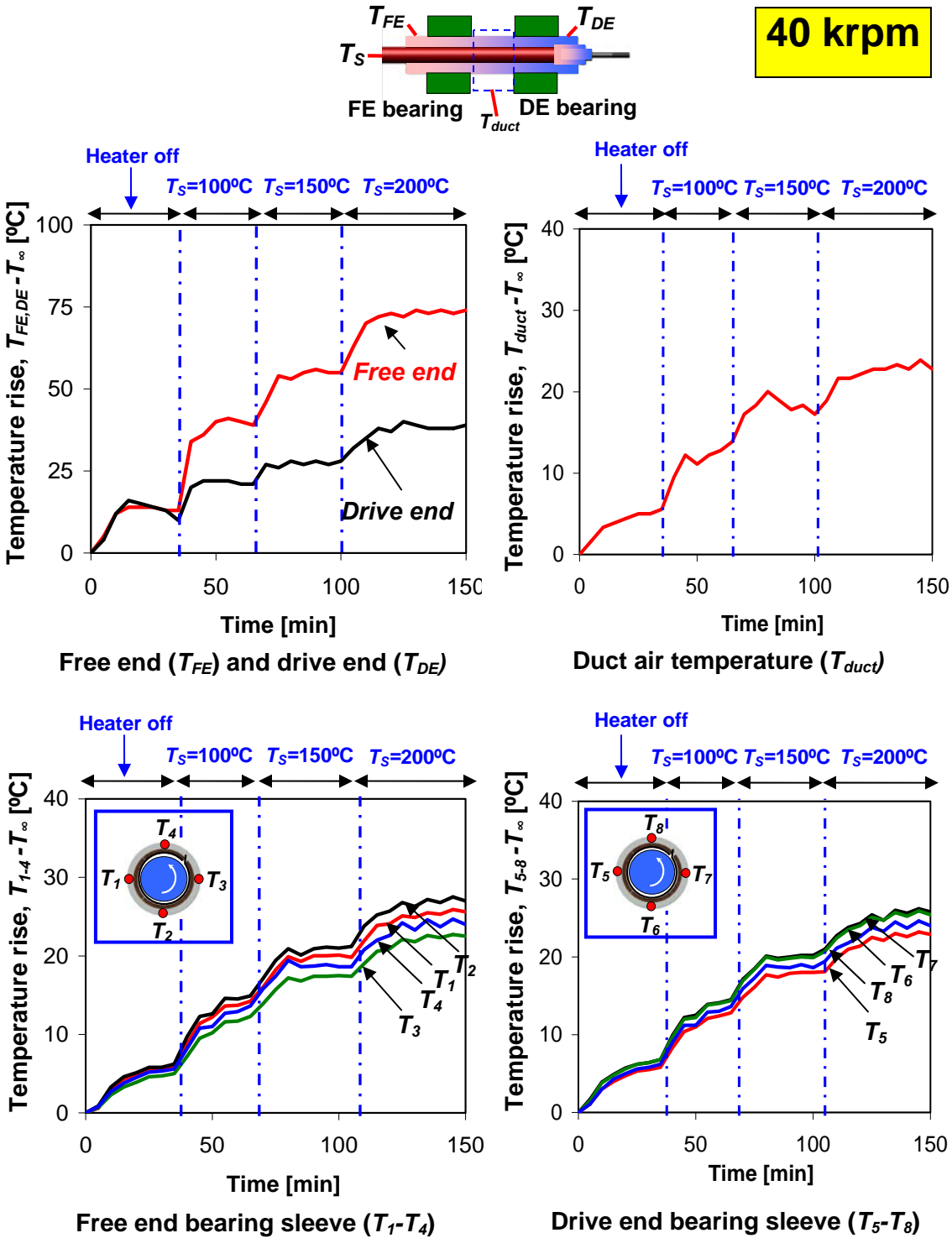


Fig. 18 Rotor spinning at 40 krpm: Recorded test system component temperature rises versus elapsed time. Steady axial cooling flow into bearings at 160 L/min

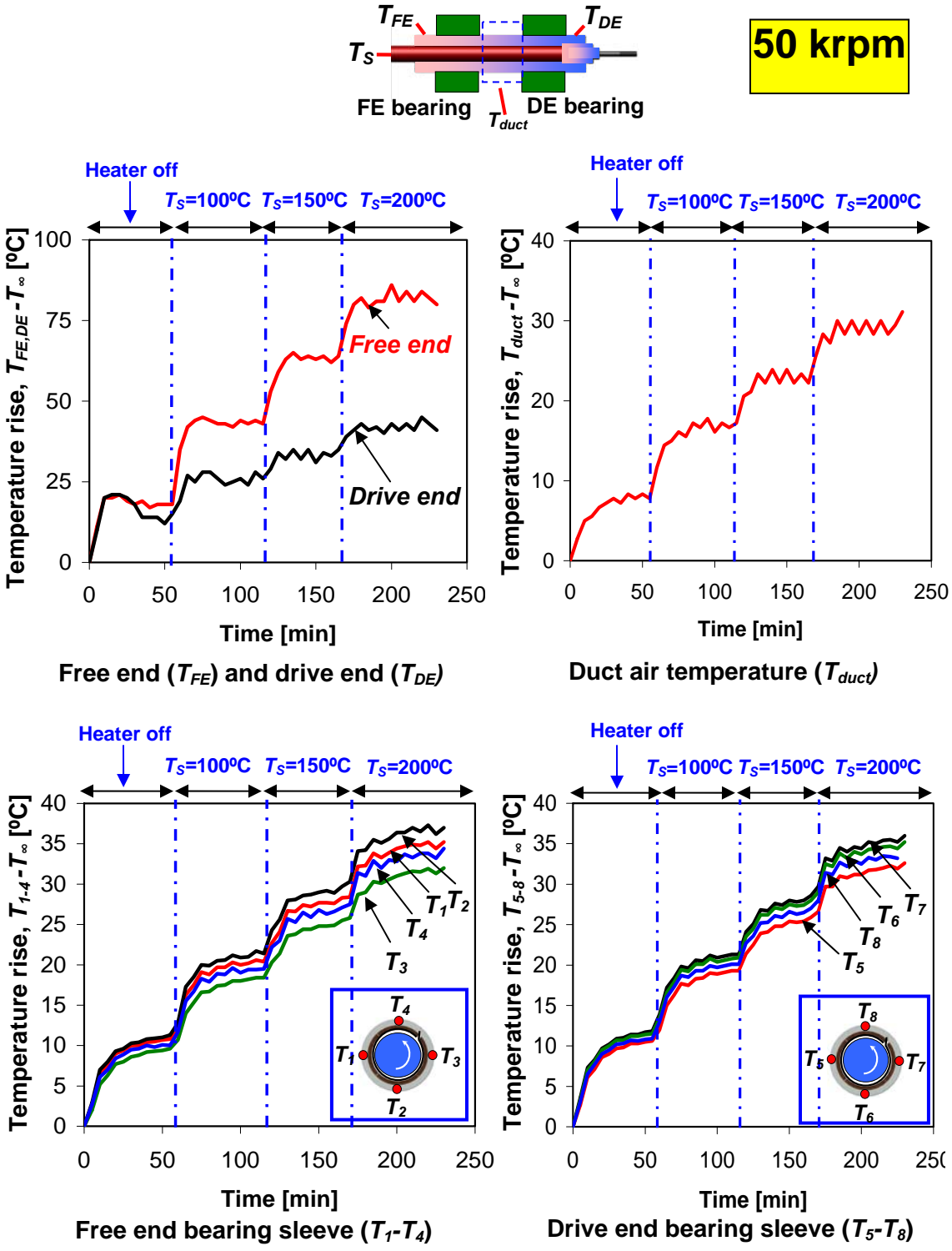


Fig. 19 Rotor spinning at 50 krpm: Recorded test system component temperature rises versus elapsed time. Steady axial cooling flow into bearings at 160 L/min

Figure 20 shows the temperature rise on the rotor surface, (a) free end and (b) drive end, for various heater set temperatures and versus rotor speed. The rotor shows a marked axial temperature gradient, more pronounced as the heater temperature increases. The rotor free end temperature rise is higher than that at the drive end since the heater has a marked temperature differential along its axis, being hotter at the rotor free end. In general, the rotor OD temperature rises as the rotor speed increases. This effect is markedly linear, in particular when the heater is not active. Note that without spinning, the rotor contacts the bearings. As the rotor starts spinning, an air gap is formed between the top foil and the rotor that aids to ‘cool’ the rotor. This effect is noticeable only for the test with the highest heater set temperature of 200 °C.

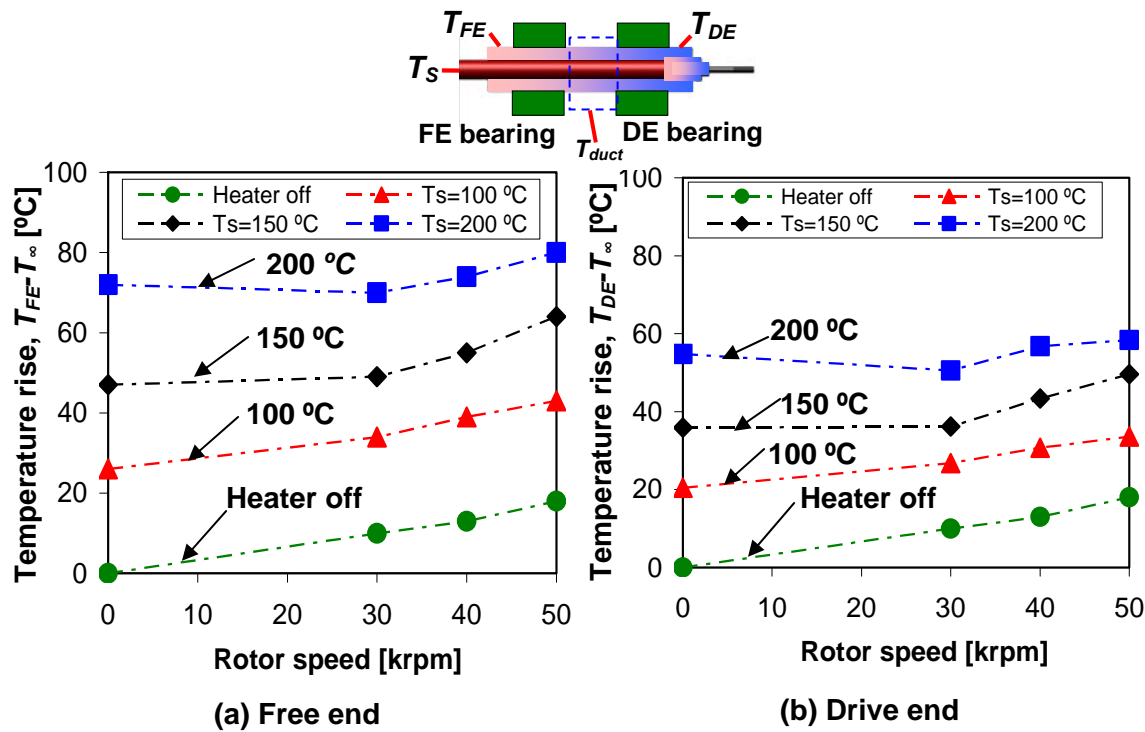


Fig. 20 Equilibrium temperatures rise at rotor OD surface, free and drive ends, versus rotor speed. Steady axial cooling flow into bearings at 160 L/min

Figure 21 shows the rotor OD temperature rises ($T_{FE}-T_{duct}$) and ($T_{DE}-T_{duct}$) with respect to the duct air temperature (T_{duct}) versus rotor speed for various heater set temperatures. Recall that there is a distinct temperature gradient along the rotor when the heater is active. The rotor temperature rises at both ends are almost identical when the heater is turned off. With the heater set temperatures at $T_s=100$ °C, 150 °C, and 200 °C, the rotor OD free end shows a much larger

increase in temperature than the rotor drive end. In general, with increasing rotor speed, the temperature rises at either of the rotor ends.

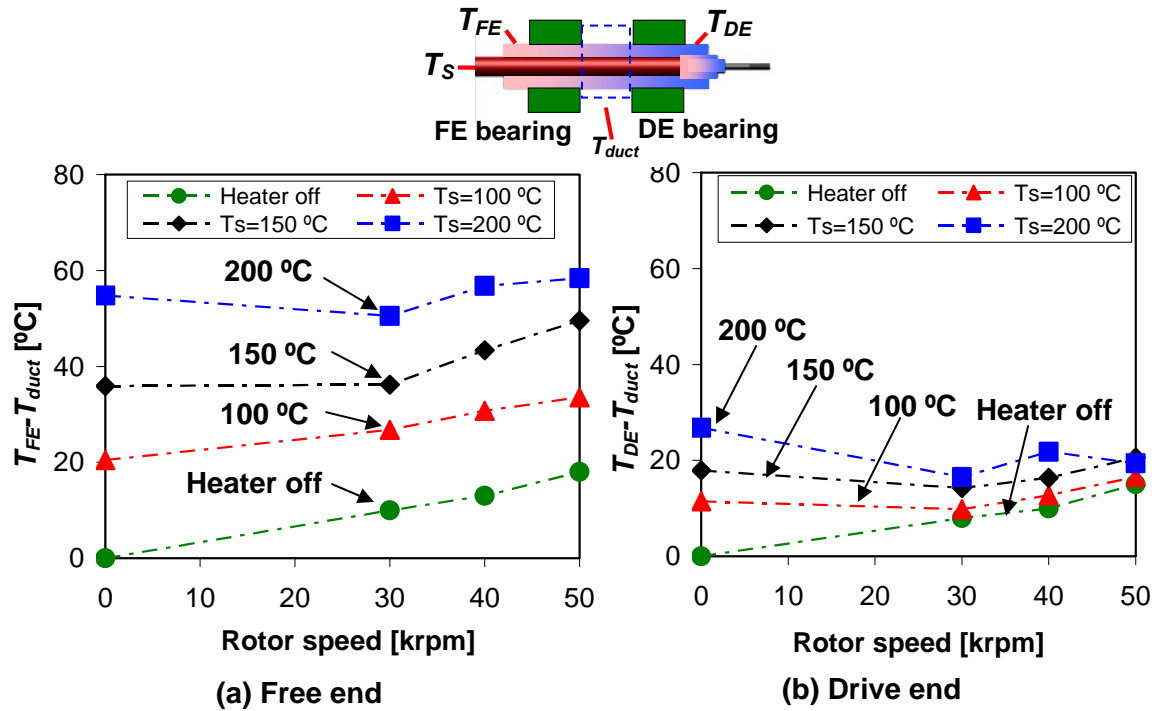


Fig. 21 Rotor temperature rise relative to the duct temperature, $(T_{FE} - T_{duct})$ and $(T_{DE} - T_{duct})$, at equilibrium versus rotor speed. Steady axial cooling flow into bearings at 160 L/min. (Note that T_{duct} increases with rotor speed)

Figure 22 depicts the bearings' OD average temperature rise ($T_{1-4} - T_{\infty}$, $T_{5-8} - T_{\infty}$) versus rotor speed and for increasing heater temperatures (T_s). Figure 23 depicts the same temperatures but relative to the duct temperature, i.e., $(T_{1-4} - T_{duct})$ and $(T_{5-8} - T_{duct})$. Note that the vertical bars in each data point show the standard deviation of the four measured temperatures on a bearing cartridge. Even though there is a significant thermal gradient along the rotor axis (max. ~ 20 °C between the two bearing locations for the highest heater set temperature), the temperature rises in the two bearings are nearly identical. The standard deviation of the temperatures around the bearing cartridge outer surface increases with increasing heater temperature. Thus, for a higher T_s , a more pronounced circumferential thermal gradient takes place around the bearing cartridge. With increasing rotor speed, from 30 krpm to 50 krpm, the bearing OD temperatures with respect to the duct temperature increase rapidly. That is, relative to the air inlet temperature, the bearings heat steadily and show a temperature rise growth proportional to rotor speed.

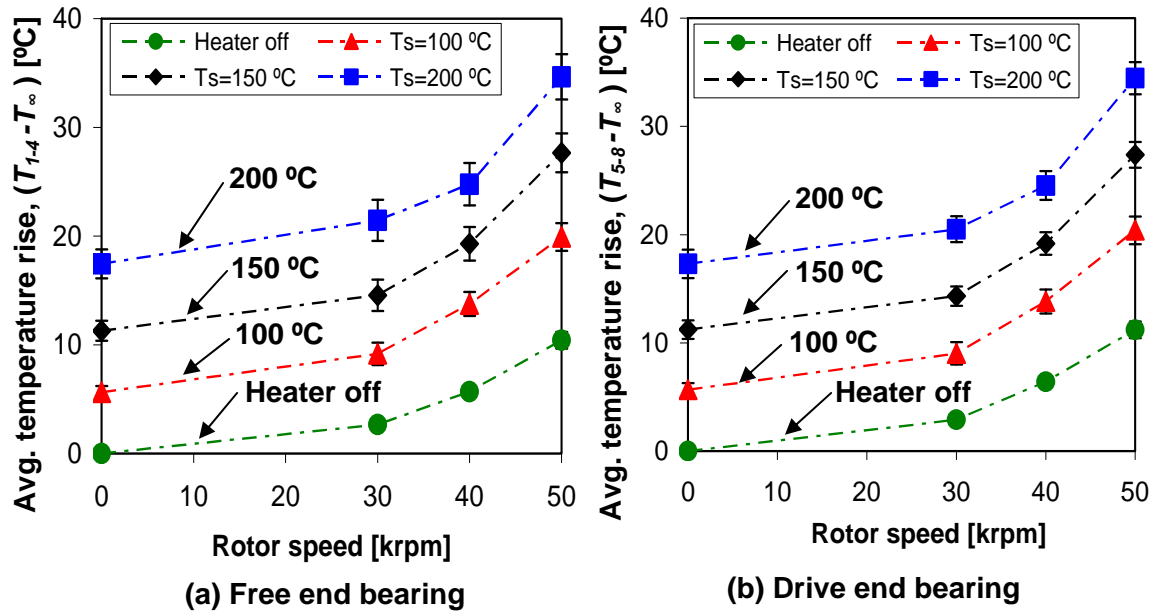


Fig. 22 Average bearing OD temperature rises (with std. deviation) versus rotor speed and increasing heater temperatures. Steady axial cooling flow into bearings at 160 L/min

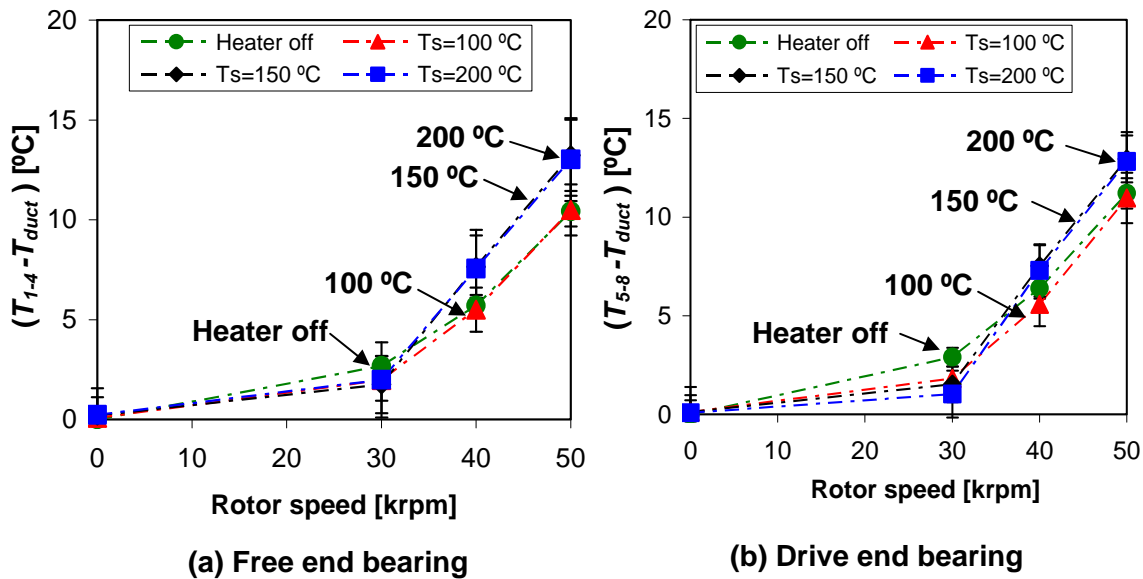


Fig. 23 Average bearing OD temperature rise with respect to duct temperature versus rotor speed and increasing heater temperatures. Steady axial cooling flow into bearings at 160 L/min

Rotordynamic measurements with rotor operating at increasing temperatures

The following measurements elucidate the effect of rotor temperature on the dynamic forced response of the test rotor. The experiments are conducted with heater set temperatures (T_S) at 22 °C (room temperature), 100 °C, 150 °C, and 200 °C. Note that as the rotor temperature increases, the rotor and bearings' material properties and geometry change. Hence, the bearings' assembly clearances also change.

Once the bearings and the rotor are assembled and the rotor balanced in place, large imbalance masses of 240 mg and 360 mg are added at the two rotor end planes for various tests. Note that the baseline response due to remnant imbalance is not subtracted in the following results. The baseline responses for the various operating temperatures are not identical. A prior section reported the rotordynamic measurements with baseline subtraction for tests conducted with the heater off. Presently, the rotor dynamic response is recorded while the rotor speeds up to 36 krpm (600 Hz) with an acceleration of 400 rpm/s (6.7 Hz/s). All experiments were conducted three times to establish the repeatability of the recorded rotor responses.

Once the electric heater is turned on, the operator waits for the system to reach a thermal equilibrium, and turns on the motor to spin the rotor to a maximum speed of 36 krpm¹¹ (600 Hz) and then the rotor is allowed to coast down to rest. The operator waits for the system to reach a thermal steady state once again before resuming a test. After three sets of identical tests, the heater set temperature is increased and the procedure repeated. The heater temperature fluctuates ± 5 °C maximum while the heater control circuit turns the heater coil on/off intermittently to maintain the set temperature. Note that the rotor and bearing cartridges' OD temperatures remain fairly constant once a thermal steady state is achieved.

Table 3 lists the steady state temperatures on the rotor surfaces (T_{FE} , T_{DE}) and at the four bearing OD locations. Figure 24 depicts the rotor surface temperatures (T_{FE} , T_{DE}) versus heater set temperatures. The rotor free and drive end equilibrium temperatures show slight variations in the repeated tests; being more pronounced when the heater set temperature is at 200 °C. The temperatures listed were measured before spinning the rotor and the operator waited for ~ 30 min

¹¹ High temperature measurements are conducted only up to a maximum speed of 36 krpm. Ambient temperature measurements are conducted to a maximum speed of 50 krpm.

between tests to achieve a thermal equilibrium. Note, however, that the tests with the heater temperature at 200°C were resumed before reaching a thermal equilibrium.

Table 3 Measured bearing cartridges and rotor OD temperatures for increasing heater set temperatures (T_s). Steady axial cooling flow into bearings at 160 L/min.

Imbalance mass	Heater set temp. T_s (°C)	Rotor free end temp. T_{FE} (°C)	$T_1 - T_4$ (°C)			Duct air, T_{duct} °C	Rotor drive end temp. T_{DE} (°C)	$T_5 - T_8$ (°C)	
			Avg. bearing OD temp.	Std. dev.				Avg. bearing OD temp.	Std. dev.
240 mg Out-of phase	Heater off	25.5	25.5	0.0	22	25.5	25.5	0.0	
	100	47±1	30.8	0.4	30	36±1	31.0	0.5	
	150	63±1	35.5	0.7	33	46±1	35.7	0.7	
	200	82±3	39.5	1.1	38	54±3	39.4	1.2	
360 mg In-phase	Heater off	24	24.0	0.0	21	24	24.0	0.0	
	100	46±1	28.7	0.5	27	32±2	28.6	0.5	
	150	68	35.2	0.9	33	47±1	35.2	0.9	
	200	92±1	41.5	1.4	37	62±1	41.3	1.3	

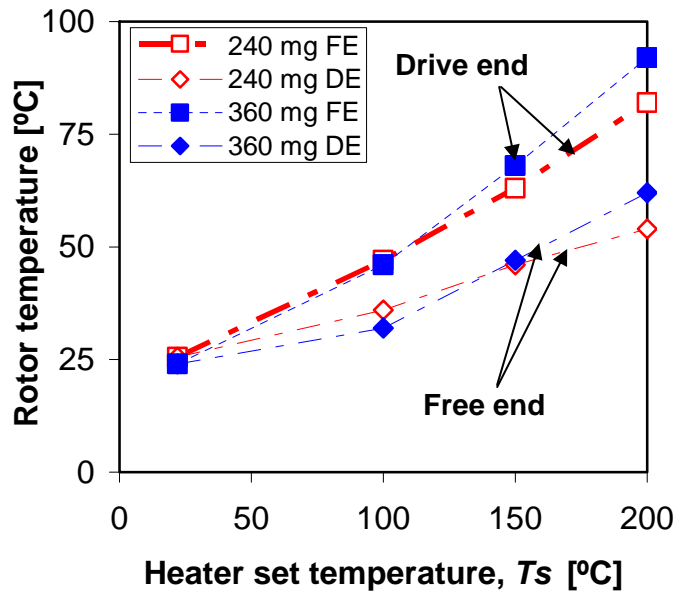
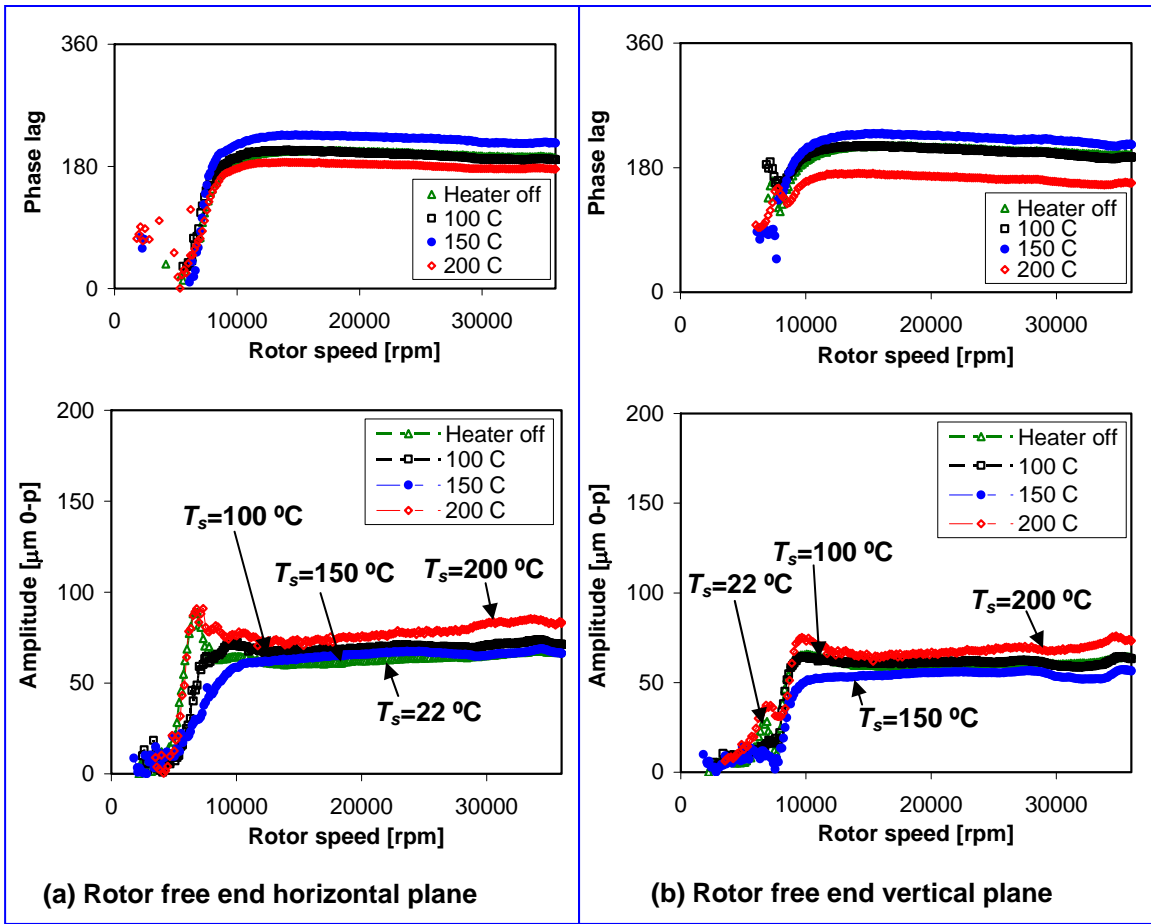


Fig. 24 Rotor OD temperatures, free and drive ends, immediately before conducting a rotor speed ramp-up test. Steady axial cooling flow into bearings at 160 L/min. Data from tests with 240mg (out-of-phase) and 360 mg (in-phase) mass imbalances.

Note that the thermal equilibrium is lost instantly as soon as the rotor starts spinning. The rotor OD surface temperatures are much lower than the heater set temperatures. Also, the bearing cartridge temperatures are smaller than the rotor surface temperatures, and hence it is reasonable to assume that the metal mesh (and top foil) temperatures fall somewhere in between the rotor and bearing cartridge temperatures.

Figure 25 shows the amplitude and phase of rotor response, near the rotor free end bearing, during controlled rotor acceleration (400 rpm/s) and with out-of-phase imbalance masses ($m_e=240$ mg) attached at the rotor end planes. Note that the rotor has a remnant imbalance even after trim balancing. The inset table shows the corresponding rotor OD surface temperatures for each heater set temperature. The rotor amplitudes along the horizontal plane peak at ~ 7 krpm, while the vertical amplitudes peak at ~ 9 krpm. Rotor slow roll is compensated at $\sim 2,300$ rpm. The heater temperature has little influence on the recorded amplitude. Note from Table 2 that the bearings OD temperatures (T_{1-4} and T_{5-8}) rise by only ~ 20 °C for the highest $T_s=200$ °C. Thus, with the set cooling flow rate at 160 liter/min, the rotor and bearing do not heat too much

Figure 26 shows a typical waterfall plot of the rotor response amplitude at the free end, horizontal plane, for a test with the heater set temperature $T_s=200$ °C. The measurements evidence no sub-synchronous vibration amplitudes, while small amplitude 2X and 3X components are present over the entire speed range.



Heater set temp, T_s (°C)	22	100	150	200
Rotor FE, T_{FE} (°C)	26	47	63	82
Rotor DE, T_{DE} (°C)	26	36	46	54

Fig. 25 Rotor synchronous response amplitude and phase versus shaft speed for out-of-phase imbalance masses = 240 mg. Measurements at rotor free end, (a) horizontal plane and (b) vertical plane. Rotor acceleration of 400 rpm/s. Cooling flow rate ~160 L/min. Inset table shows average rotor OD temperatures corresponding to each heater set temperature

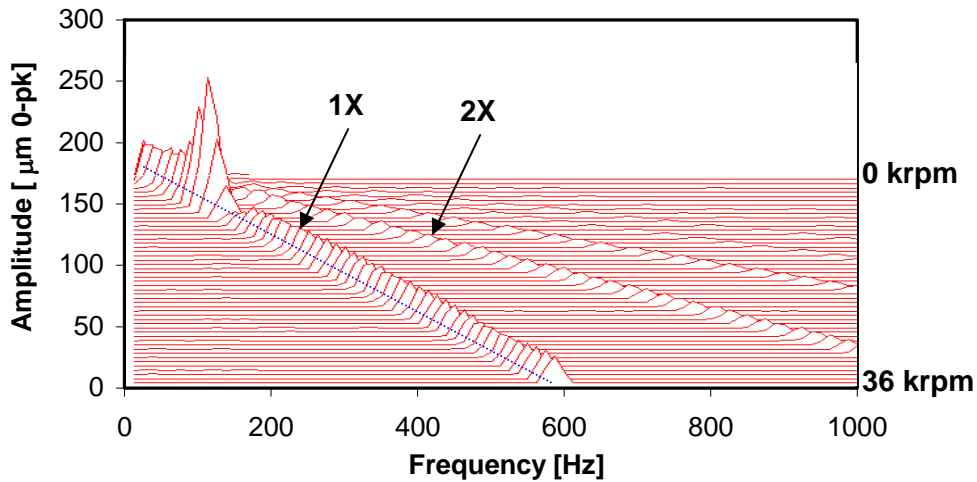
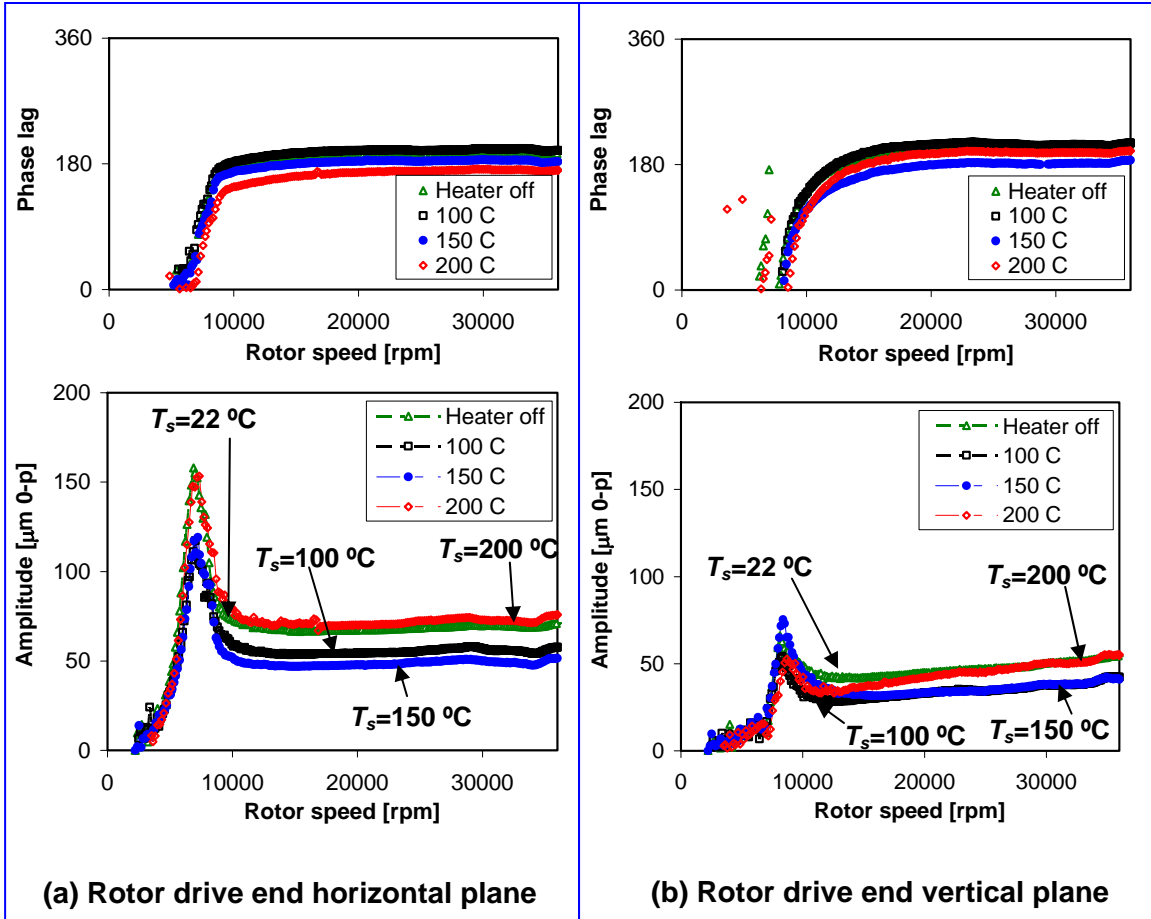


Fig. 26 Waterfall plot of rotor response at the rotor free end, horizontal plane, for out-of-phase imbalance masses = 240 mg. Rotor acceleration 400 rpm/s. Heater set temperature = 200 °C. Cooling flow rate ~160 L/min.

In general, the rotor lateral displacements show only a single peak as it accelerates to the top speed of 36 krpm. A one DOF (degree of freedom) model may be used to estimate effective stiffness coefficients, K_{eff} , from the measured rotor radial displacements. The natural frequency (ω_n), corresponding to the phase angle of 90° and the fraction of the rotor mass (M) supported by the bearing readily provides an estimate of the effective stiffness as $K_{eff} = \omega_n^2 M$. Here, along the horizontal direction, $\omega_n \sim 732$ rad/s (7 krpm), and along the vertical direction, $\omega_n \sim 942$ rad/s (9 krpm).

The fraction of the weight of the rotor acting at the free end bearing is 0.58 kg (5.7 N). Thus, the effective bearing stiffness (K_{eff}) along the horizontal direction is ~ 0.31 MN/m and that along the vertical direction is ~ 0.51 MN/m.

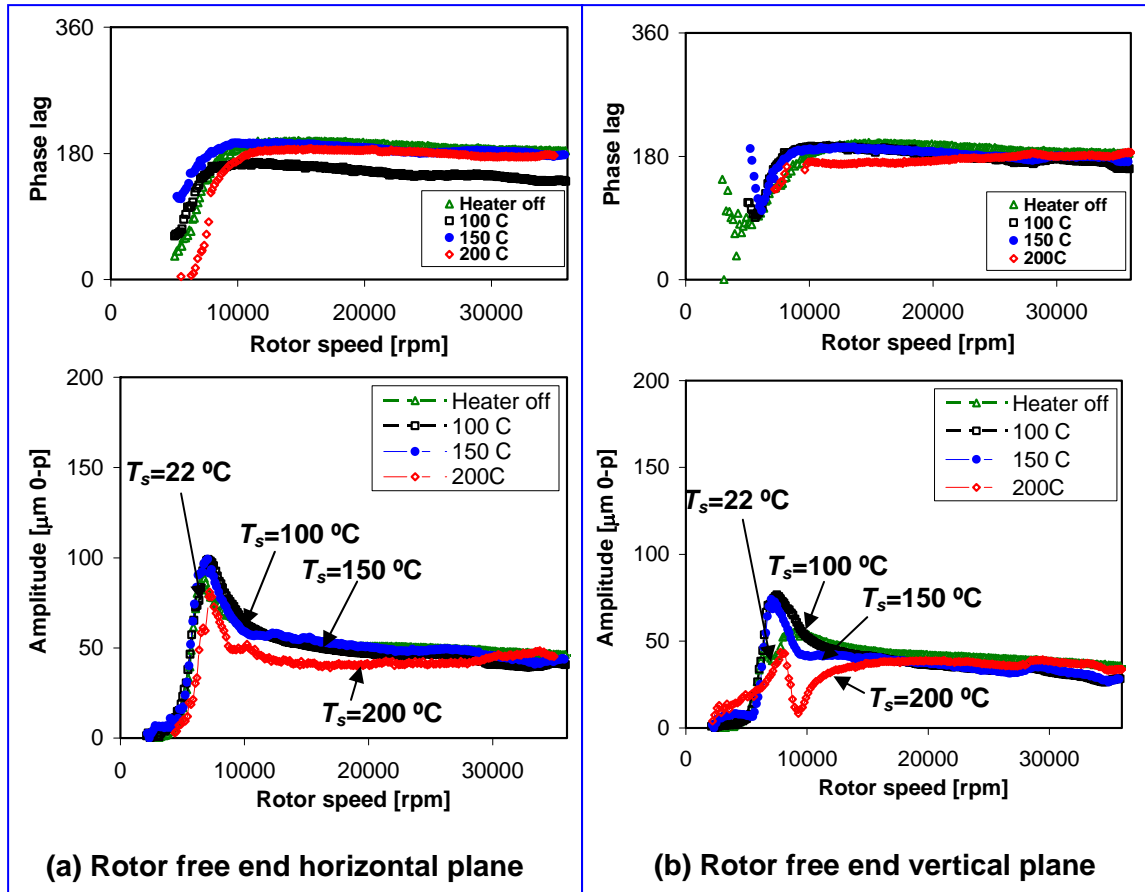
Figure 27 shows the amplitude and phase of the rotor response, near the rotor drive end bearing. Out-of-phase imbalance masses equaling 240 mg are attached at the rotor end planes. The response at the rotor drive end shows that, along the horizontal direction, $\omega_n \sim 732$ rad/s (7 krpm), and along the vertical direction, $\omega_n \sim 942$ rad/s (9 krpm). The fraction of the rotor load acting at the drive end bearing is 0.75 kg. Thus, the effective bearing stiffness (K_{eff}) along the horizontal direction is ~ 0.40 MN/m and that along the vertical direction is ~ 0.66 MN/m.



Heater set temp, T_s °C	22	100	150	200
Rotor FE °C	25	47	63	82
Rotor DE °C	25	36	46	54

Fig. 27 Rotor synchronous response amplitude and phase versus shaft speed for out-of-phase imbalance masses = 240 mg. Measurements at rotor drive end (a) horizontal plane and (b) vertical plane. Rotor acceleration of 400 rpm/s. Cooling flow rate ~160 L/min. Inset table shows average rotor OD temperatures corresponding to each heater set temperature

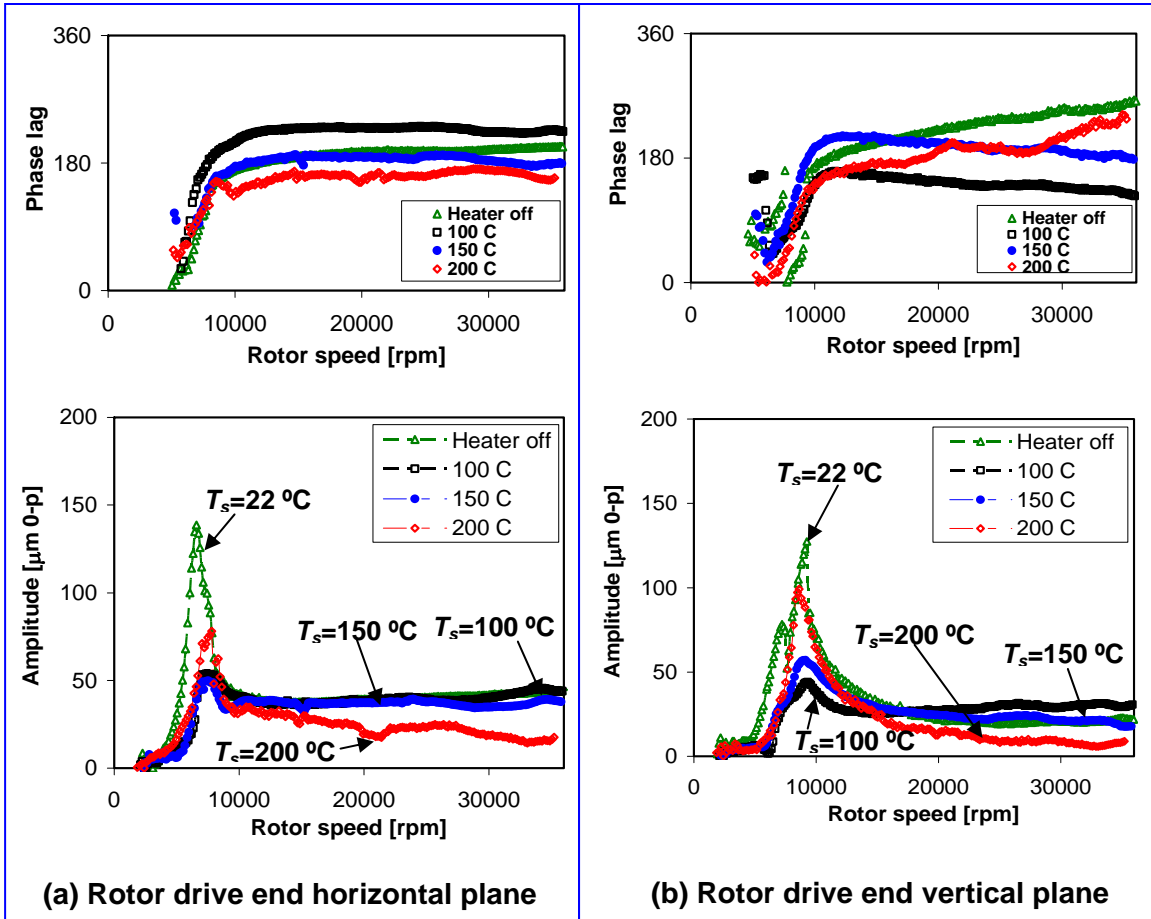
Figures 28 and 29 depict the amplitudes (V & H) and phase angles of rotor response, near its free end and drive end, respectively, during a controlled speed ramp rate of 400 rpm/s and with in-phase imbalance masses equaling 360 mg attached at the rotor end planes. The rotor amplitude measurements for all temperatures are fairly comparable; except for the notorious dip at ~9krpm, in the rotor free end vertical displacements with the heater set temperature at 200 °C.



Heater set temp, T_s °C	22	100	150	200
Rotor FE °C	24	46	68	92
Rotor DE °C	24	32	47	62

Fig. 28 Rotor synchronous response amplitude and phase versus shaft speed for in-phase imbalance masses = 360 mg. Measurements at rotor free end (a) horizontal plane and (b) vertical plane. Rotor acceleration of 400 rpm/s. Cooling flow rate ~160 L/min. Inset table shows average rotor OD temperatures corresponding to each heater set temperature

For the largest in-phase imbalance masses (360 mg), Figure 29 shows the amplitude and phase of motion at the drive end, vertical and horizontal planes. Both at room temperature (heater off) and at the highest heater temperature (200 °C), the rotor displacements are the largest while crossing the critical speed



Heater set temp, T_s °C	22	100	150	200
Rotor FE °C	24	46	68	92
Rotor DE °C	24	32	47	62

Fig. 29 Rotor synchronous response amplitude and phase versus shaft speed for in-phase imbalance masses = 360 mg. Measurements at rotor drive end (a) horizontal plane and (b) vertical plane. Rotor acceleration of 400 rpm/s. Cooling flow rate ~160 L/min. Inset table shows average rotor OD temperatures corresponding to each heater set temperature

The waterfall plot of rotor response, depicted in Figure 30, displays peak amplitudes at ~ 116 Hz (7 krpm) and small amplitude subsynchronous motion at ~150 Hz (9 krpm) as the rotor speeds up beyond its critical speed. The data does not offer discernable trends for a conclusion to be advanced.

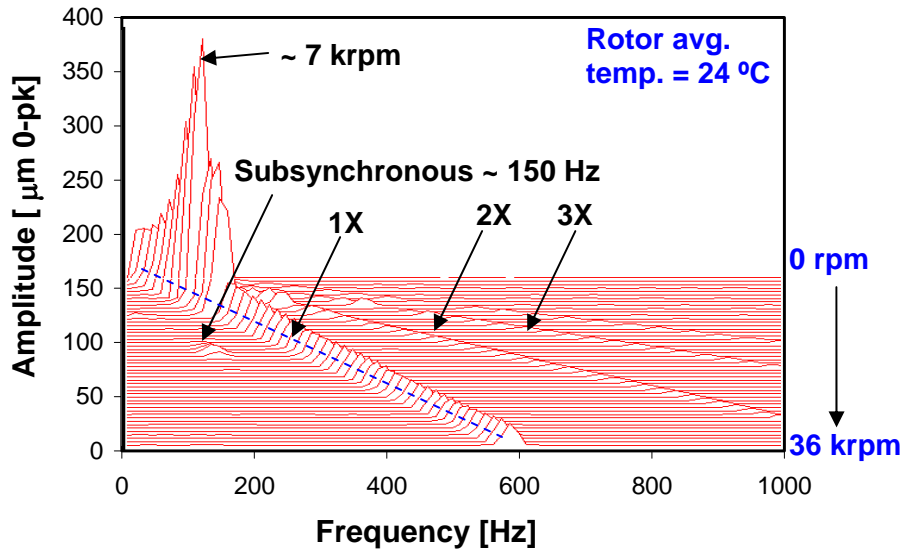


Fig. 30 Waterfall plot of rotor response at drive end, horizontal plane, with heater turned off (ambient temperature). Rotor acceleration 400 rpm/s. In-phase imbalance masses = 360 mg. Cooling flow rate ~160 L/min.

Figure 31 displays the waterfall plot of rotor response amplitude at the rotor drive end, vertical plane, with the heater (a) turned off and (b) with a set temperature of 200 °C. While the waterfall plots for the imbalance mass of 240 mg out-of-phase displayed no sub-synchronous amplitudes, the present waterfall for a larger imbalance mass of 360 mg in-phase shows sub-synchronous motion amplitudes at ~150 Hz. Again, for the highest heater set temperature of 200 °C, the sub-synchronous motion is more pronounced. The measurements also show 2X and 3X vibration components, albeit with a very small magnitude.

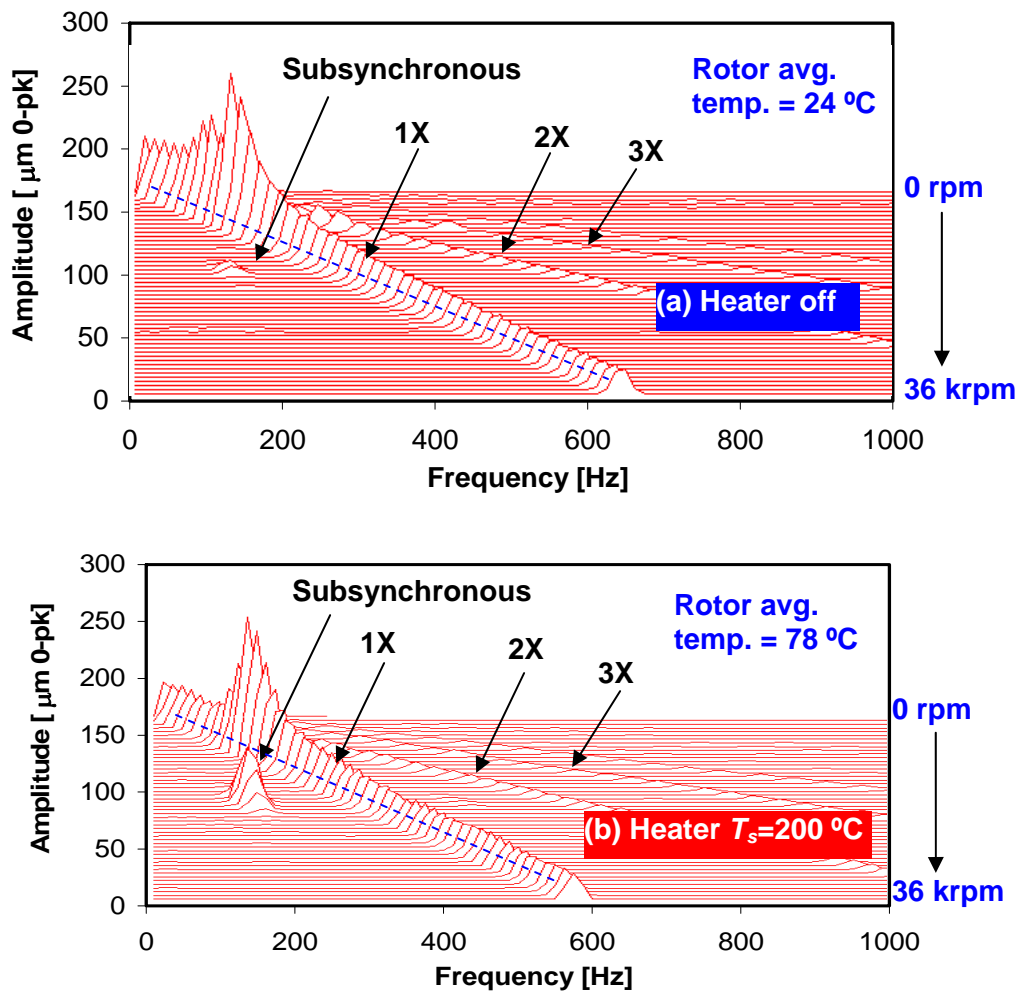


Fig. 31 Waterfall plot the rotor response at the rotor drive end, vertical plane, for (a) heater turned off, and (b) heater set temperature = 200 °C. Rotor acceleration 400 rpm/s. In-phase imbalance masses = 360 mg. Cooling flow rate ~160 L/min.

Conclusions

The implementation of metal mesh foil bearings (MMFBs) in high temperature applications requires proper characterization of their thermal behavior, i.e., to demonstrate adequate thermal management. The report presents rotordynamic measurements of a rotor supported on a pair of MMFBs constructed in the laboratory ($L=38.10$ mm, $D=36.58$ mm). The tests consist of heating the hollow rotor using an electric cartridge heater at set temperatures equaling 100 °C, 150 °C, and 200 °C and recording rotor surface and bearing OD temperatures, as well as rotor dynamic displacements, while the rotor spins at 30 krpm, 40 krpm, and 50 krpm, and also during transient rotor speed up and coast down tests to 50 krpm

A finite element structural analysis of the rotor with force coefficients predicted for the MMFB delivers rotor responses for in-phase and out-of-phase imbalance masses, as in the tests. Normalized amplitudes of the recorded rotor responses show the system behaves linearly up to 50 krpm. Waterfall plots show dominant synchronous response motions, with small amplitude 2X and 3X motions. The predictions agree well with the recorded displacements albeit there are marked differences in the peak amplitudes when the rotor crosses its critical speeds – the test bearings show lesser damping than predictions indicate.

In the tests with the heater set to a high temperature (max. 200 °C), the rotor and bearing OD temperatures increase by 70°C and 25°C, respectively. Most rotor dynamic responses do not show a marked difference for operation under cold (ambient temperature) and hot rotor conditions. Note that a steady inlet air flow rate at ~ 160L/min is provided continuously to cool the bearings.

The rotor and bearings survived numerous start up-shutdown events, and steady speed operation for several hours, with added imbalance masses as large as 360 mg ($u=22.6$ μm) at 50 krpm speed and 200 °C heater temperature (~ max. 100 °C at the rotor OD). With an abundant cooling flow rate (160 LPM), the performance of the test bearings is not significantly affected by increasing rotor temperatures.

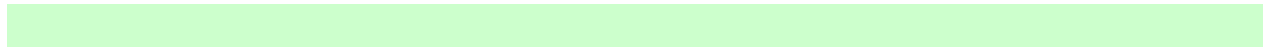
The effect of varying the air cooling flow rate was not investigated; prior research in the authors' laboratory shows that the cooling air supply is important for the safe operation of foil bearing supported rotors, particularly for operation at high temperatures.

Nomenclature

$C_{\alpha\beta}, C$	Damping coefficients; $\alpha, \beta = X, Y$ [N·s/m]
c	Radial clearance [m]
D	Top foil (bearing) diameter, $D = 2 \times R$ [m]
D_o, D_i	Rotor outer and inner diameter [m]
I	Moment of inertia [kg m ²]
K_{eff}	Effective stiffness coefficient [N/m]
$K_{\alpha\beta}, K$	Stiffness coefficients; $\alpha, \beta = X, Y$ [N/m]
L	Bearing axial width [m]
M	Rotor mass [kg]
m_e	Imbalance mass [kg]
N	Rotor speed [rpm]
R	Top foil (bearing) radius [m]
r	Radius for location of imbalance masses [m]
T_s	Heater set temperature [°C]
$T_i, i=1-4, 5-8$	Bearing cartridge (OD) temperatures at rotor free end and drive end [°C]
$T_{FE,DE}$	Rotor free end and rotor drive end temperatures [°C]
T_{duct}	Inlet duct air temperature [°C]
u	Rotor center imbalance displacement [μ m]
W	Applied load [N]
x, y	Coordinate system [m]
γ	Structural damping loss factor [-]
ω	Frequency [rad/s]
ω_n	Natural frequency [rad/s]

References

- [1] Valco, M.J. and DellaCorte, C., 2003, "Emerging Oil-Free Turbomachinery Technology for Military Propulsion and Power Applications," *Proc. ARMY Sciences Conf.*, Ft. Lauderdale, FL.
- [2] Barnett, M.A., and Silver, A., 1970, "Application of Air Bearings to High-Speed Turbomachinery," SAE Paper No. 700720.
- [3] Peng, Z.-C., and Khonsari, M.M., 2004, "Hydrodynamic Analysis of Compliant Foil Bearings with Compressible Air Flow," *ASME J. Tribol.*, **126**(3), pp. 542-546.
- [4] San Andrés, L., Chirathadam, T.A., and Kim, T.H., 2010, "Measurement of Structural Stiffness and Damping Coefficients in a Metal Mesh Foil Bearing," *ASME J. Eng. Gas Turbines Power*, **132**(3), p. 032503.
- [5] DellaCorte, C., Radil, K.C., Bruckner, R.J., and Howard, S.A., 2008, "Design, Fabrication, and Performance of Open Source Generation I and II Compliant Hydrodynamic Gas Foil Bearings," *Tribol. Transactions*, **51**, pp. 254-264.
- [6] Kim, T.H., and San Andrés, L., 2006, "Limits for High Speed Operation of Gas Foil Bearings," *ASME J. Tribol.*, **128**, pp. 670-673.
- [7] Ao, H., Jiang, H., Wei, W., and Ulanov, A.M., 2006, "Study on the Damping Characteristics of MR Damper in Flexible Supporting of Turbo-Pump Rotor for Engine," *Proc. 1st Symposium on Systems Control in Aerospace and Astronautics*, Harbin, China, Jan. 19-21, pp. 618-622.
- [8] Ertas, B.H., Al-Khateeb, E.M., and Vance, J.M., 2003, "Rotordynamic Bearing Dampers for Cryogenic Rocket Engine Turbopumps," *AIAA J. Propul. Power*, **119**(4), pp. 674-682.
- [9] Choudhry, V., and Vance, J.M., 2005, "Design Equations for Wire Mesh Bearing Dampers in Turbomachinery," ASME Paper No. GT 2005-68641.
- [10] Kim, T.H., Breedlove, A.W., and San Andrés, L., 2009, "Characterization of Foil Bearing Structure for Increasing Shaft Temperatures: Part I-Static Load Performance," *ASME J. Tribol.*, **131**(4), p.041703.

- [11] San Andrés, L., Kim, T.H., Ryu, K., Chirathadam, T. A., Jarrett, C., Hagen, K., Martinez, A., Rice, B., Niedbalski, N., Hung, W., and Johnson, M., “ Gas Bearing Technology for Oil-Free Microturbomachinery – Research Experience for Undergraduate (REU) Program at Texas A&M University,” ASME Paper No. GT2009-59920.
- [12] San Andrés, L., Kim, T.H., Chirathadam, T.A., and Ryu, K., 2010, “Measurements of Drag Torque, Lift-Off Journal Speed and Temperature in a Metal Mesh Foil Bearing,” ASME J. Eng. Gas Turbines Power, **132**(11), p. 112503.
- [13] Chirathadam, T., 2012, “Metal Mesh Foil Bearings: Prediction and Measurement of Static and Dynamic Performance Characteristics”, Ph.D Dissertation, Texas A&M University, College Station, TX
- [14] San Andrés, L., Kim, T.H., and Ryu, K., 2010, “Thermal Management and Rotordynamic Performance of a Hot Rotor-Gas Foil Bearings System: Part 1- Measurements,” ASME J. Eng. Gas Turbines Power, **133** (June), 062501.
- [15] Ryu, K., 2011, “Effect of Cooling Flow on the Operation of a Hot Rotor-Gas Foil Bearing System,” Ph.D Dissertation, Texas A&M University, College Station, TX.
- 

Appendix A. Manufacturing a metal mesh foil bearing

A metal mesh foil bearing (MMFB), as depicted in Figure A.1 comprises of three components, (a) a bearing cartridge, (b) one or more compressed metal mesh pads, and (c) a pre-formed top foil. This section describes the manufacturing procedure for the components of a MMFB.

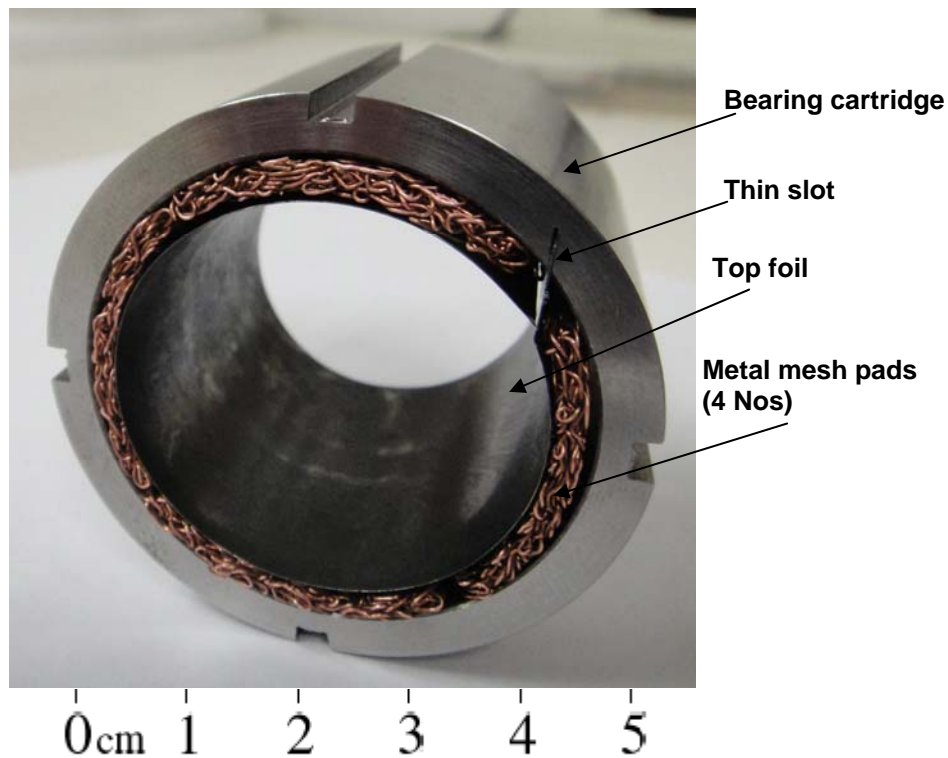


Fig. A.1 Metal mesh foil bearing with four metal mesh pads

Bearing Cartridge The bearing cartridge is an annular cylindrical shell, typically made of stainless steel, and has a thin slot on the inner surface for affixing one of the top foil ends. The thin slot, machined using electrical discharge machining (EDM) method, is wide enough for top foil slide fit. Further, the top foil is secured in place using set screws threaded into the bearing cartridge from the outer surface. Figure A.2 illustrates the details of the slot on bearing cartridge and the dimensions for the test bearing reported in the main body of the report (Table 1).

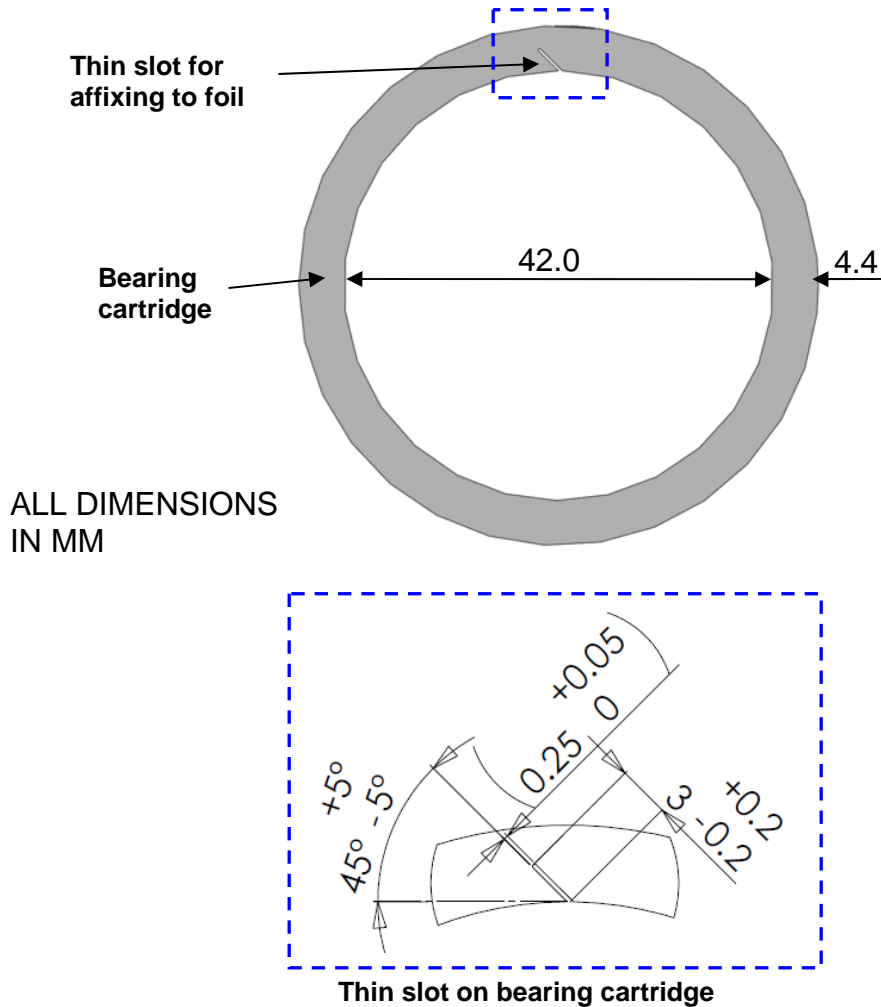


Fig. A.2 Bearing cartridge with a thin slot for affixing top foil. Inset shows the details of the thin slot

Top Foil The top foil is a smooth curved metal strip that is heat treated for desirable properties. The top foil, depicted in Figure A.3, is manufactured from a hard cold Rolled steel strip of Chrome-Nickel alloy steel (Rockwell 40/45) of 120 μm thickness. The dimensions of the top foil are chosen according to the desired bearing inner diameter and axial length. As the cold rolled steel strip shows considerable resistance to deformation, annealing at high temperature is required to curve it into the desired diameter.



Fig. A.3 Top foil before assembly in a MMFB. The inner surface of the top foil coated with MoS₂

Figure A.4 shows a practical arrangement for heat treating the top foil. The apparatus consists of a steel strip wrapped around the cartridge of an electric heater and wrapped tightly with clamps. The top foil is heat treated $\sim 450^\circ\text{C}$ for nearly two hours and then allowed to cool in room temperature condition. The top foil after cooling retains its arcuate shape, and has the desirable strength properties. Note that, prior efforts to heat treat the top foil at temperatures as high as $\sim 800^\circ\text{C}$ made the foils considerably brittle. One end of the top foil is slightly bent for easy installation in to the thin slot in the bearing cartridge. Although the top foil end may be bent before the heat treatment process, for proper clamping of the top foil to the heater coil, it is recommended to bend the end of the top foil later.

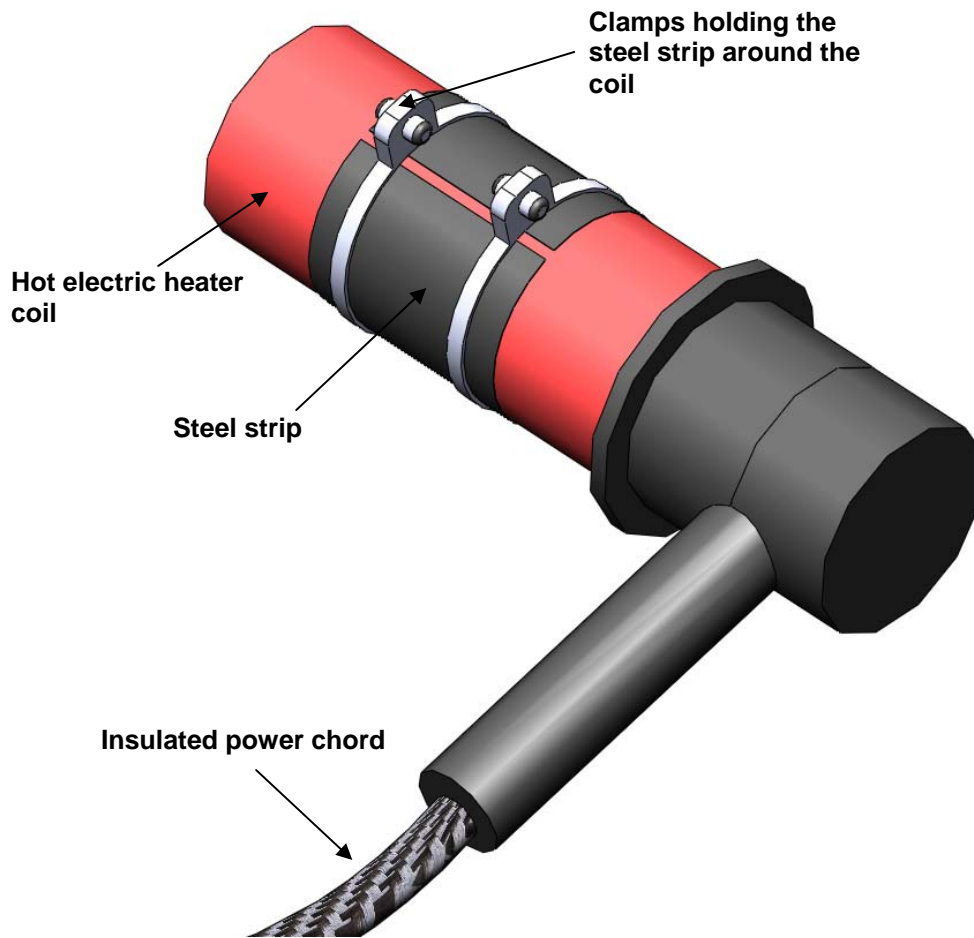


Fig. A.4 Heat treatment of the top foil wrapped around a hot heater cartridge

Metal mesh pad The compressed metal mesh structure can be a ring [4], a single flat strip curved to fit in a bearing cartridge [12], or multiple pads arranged along the bearing circumferential direction. The latest MMFB design employs multiple mesh pads as they are easier to manufacture and provides better dimensional control. The following section describes the manufacture of metal mesh pads, each spanning 90 ° arc width in a bearing. The metal mesh pad length equals the bearing axial length.

The metal mesh compactness (density) largely determines the bearing stiffness and damping. For instance, a 20 % compact metal mesh pad requires copper wires of total mass = (Volume of each pad) x (Density of copper) x (20/100). The required amount of copper wires (or copper gauze) is stacked inside an ad-hoc die made of Plexiglas, as depicted in Figure A.5, and compressed under large loads for extended amount of time. The ad-hoc die consists of a hydraulic press (not shown), a Plexiglas fixture, a metal plate equaling the desired size of the

metal mesh pad, and copper wires (or gauze). Once the compression load is removed, the metal mesh slightly grows larger in thickness due to the memory effect. Hence, several iterations are required until the desired thickness is achieved.

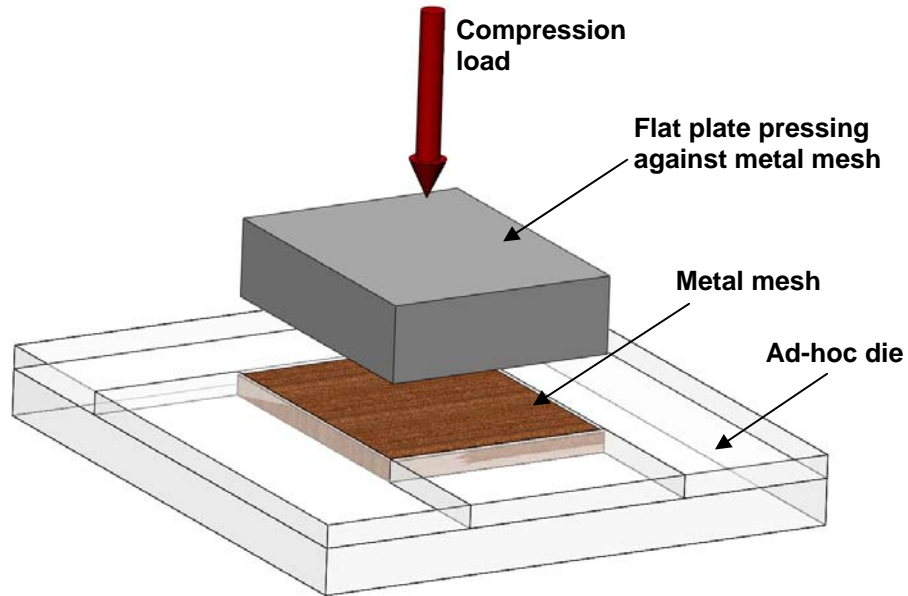


Fig. A.5 Compressing metal mesh gauze into a flat strip in an ad-hoc die

Figure A.6 shows the test setup to convert the flat metal mesh pads to an arcuate shape. The flat metal mesh pad, prepared in a die shown in Figure A.5, is placed inside a concave steel block, prepared using a hollow steel pipe of the required inner diameter. A steel cylinder with inner diameter equal to the desired metal mesh pad inner diameter is placed on top of the metal mesh pad. Then compression load is applied in a hydraulic press for several hours (typically 2-3 hours). Upon the removal of the load, the pad retains its arcuate shape.

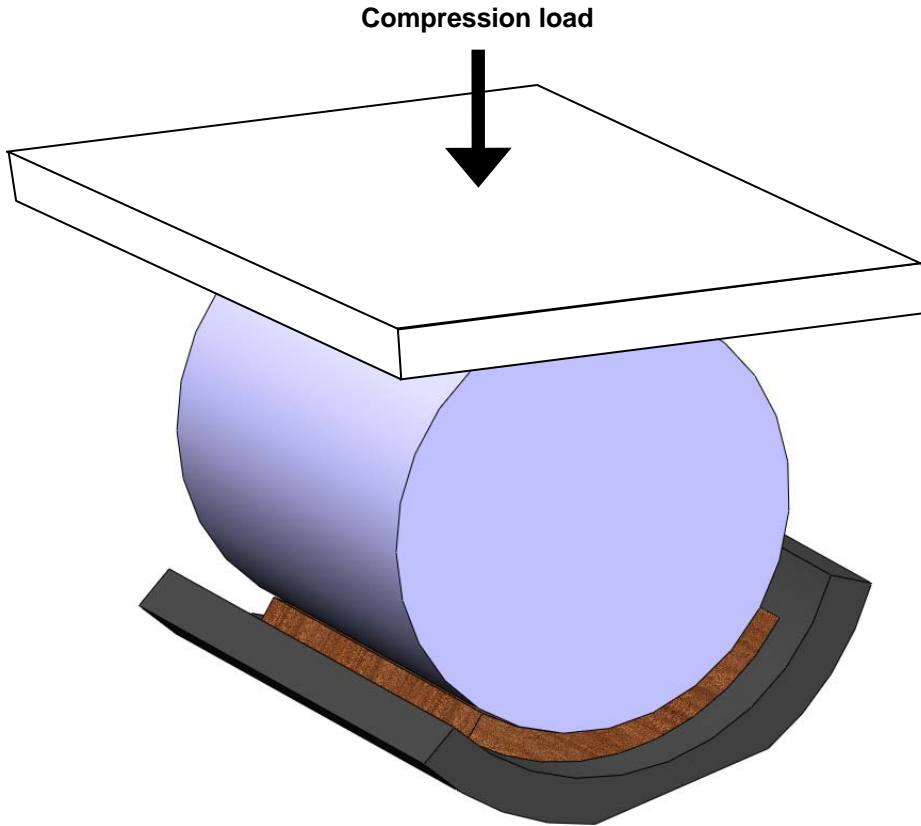
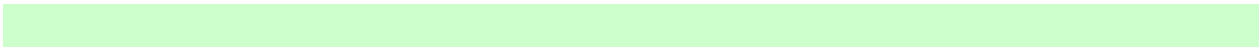


Fig. A.6 Compressing flat metal mesh strip into arcuate mesh pads



Appendix B. MMFB stiffness and damping coefficients for rotordynamic response predictions

Chirathadam [13] advances an analysis interfacing the finite element structural model of the top foil and metal mesh to the hydrodynamic gas film model governed by the lubrication Reynolds equation and predicts MMFB static performance and dynamic force coefficients. The metal mesh layer is modeled as a uniformly distributed stiffness beneath the top foil with a material loss factor (γ) representing the structural mechanical energy dissipation. Figure B.1 shows the test bearing coordinate system, with the static load acting along the Y direction. Small amplitude journal motions about an equilibrium position determine the bearing stiffness and damping force coefficients, both frequency dependent.

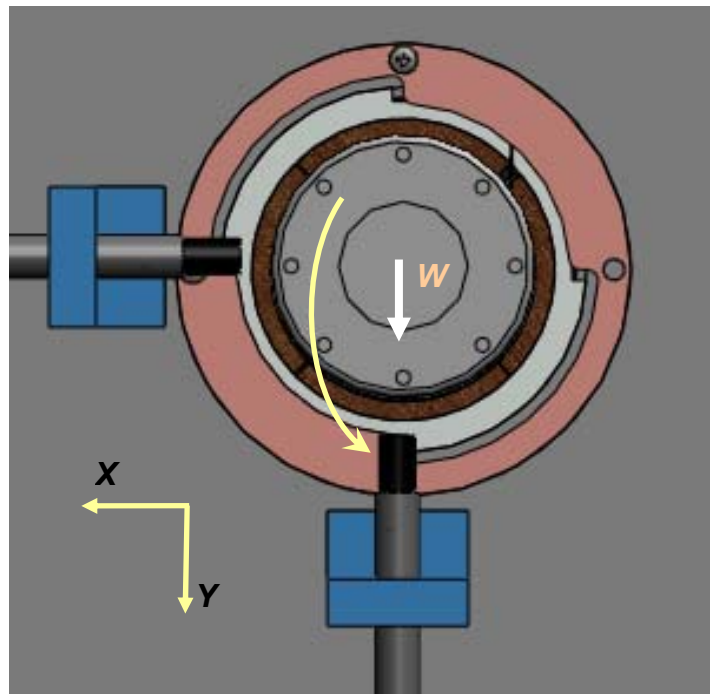


Fig. B.1 Depiction of coordinate system for analysis. Eddy current sensors recording rotor displacement along X and Y directions. Static load applied along Y direction

Table 1 (page 9, main text) gives the test bearings geometry and materials. Table B.1 and B.2 list the predicted MMFB synchronous stiffness and damping coefficients, for the rotor free drive end and free end bearings. Figure B.2 depicts the predicted MMFB synchronous speed stiffness and damping coefficients for the MMFB at the rotor drive end.

XLTRC² software includes the bearing force coefficients and predicts the rotor-bearing system synchronous response for known imbalance masses.

Table B.1 Predicted synchronous speed stiffness and damping coefficients for metal mesh bearing on rotor drive end (DEB). Static load = 7.4 N

Speed rpm	K_{XX} N/m	K_{XY} N/m	K_{YX} N/m	K_{YY} N/m	C_{XX} N-s/m	C_{XY} N-s/m	C_{YX} N-s/m	C_{YY} N-s/m
10000	587,000	-19,000	-114,000	598,000	368.9	-192.1	59.6	291.6
15000	691,000	-33,700	-80,800	614,000	272.5	-160	30.7	202.6
20000	767,000	-55,800	-62,100	628,000	211.4	-133.7	15	155.4
25000	837,000	-92,300	-60,800	644,000	169.3	-115.5	4	132.6
30000	891,000	-126,000	-64,000	662,000	139.3	-99.2	-2.2	116.7
35000	936,000	-159,000	-71,400	681,000	117.1	-85.9	-5.9	105.5
40000	971,000	-185,000	-77,100	699,000	100.5	-74.7	-7.8	95.7
45000	1,000,000	-209,000	-84,500	717,000	87.5	-65.6	-8.9	88.2
50000	1,020,000	-229,000	-90,000	733,000	77.2	-58	-9.4	81.3

Table B.2 Predicted synchronous speed stiffness and damping coefficients for metal mesh bearing on rotor free end (FEB). Static load = 5.7 N

Speed rpm	K_{XX} N/m	K_{XY} N/m	K_{YX} N/m	K_{YY} N/m	C_{XX} N-s/m	C_{XY} N-s/m	C_{YX} N-s/m	C_{YY} N-s/m
10000	555,000	4,230	-97,700	554,000	385.5	-209.2	75.2	292.5
15000	674,000	-22,600	-64,200	584,000	283.3	-172.1	36.9	206.7
20000	750,000	-44,100	-38,500	603,000	219.8	-138.5	19.4	154.8
25000	823,000	-80,700	-35,500	621,000	176.3	-118	6.1	131
30000	880,000	-114,000	-37,900	640,000	145.5	-100.9	-1.4	114.8
35000	925,000	-143,000	-42,500	659,000	122.8	-87	-5.6	102.5
40000	962,000	-170,000	-48,300	676,000	105.6	-75.8	-8	92.9
45000	1,010,000	-226,000	-84,100	715,000	88	-67.1	-9.4	92.4
50000	1,030,000	-247,000	-91,900	734,000	77.5	-59.1	-9.9	85.5

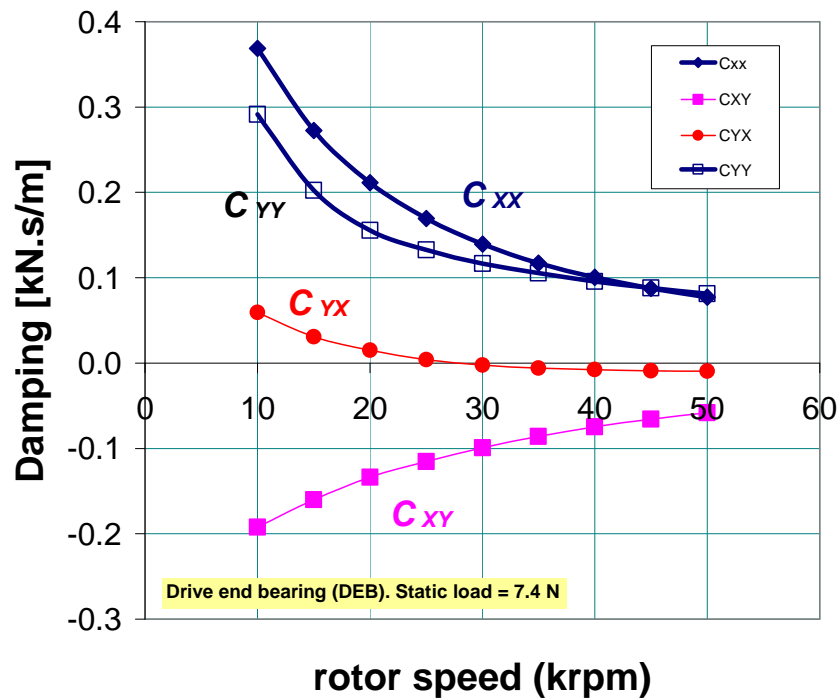
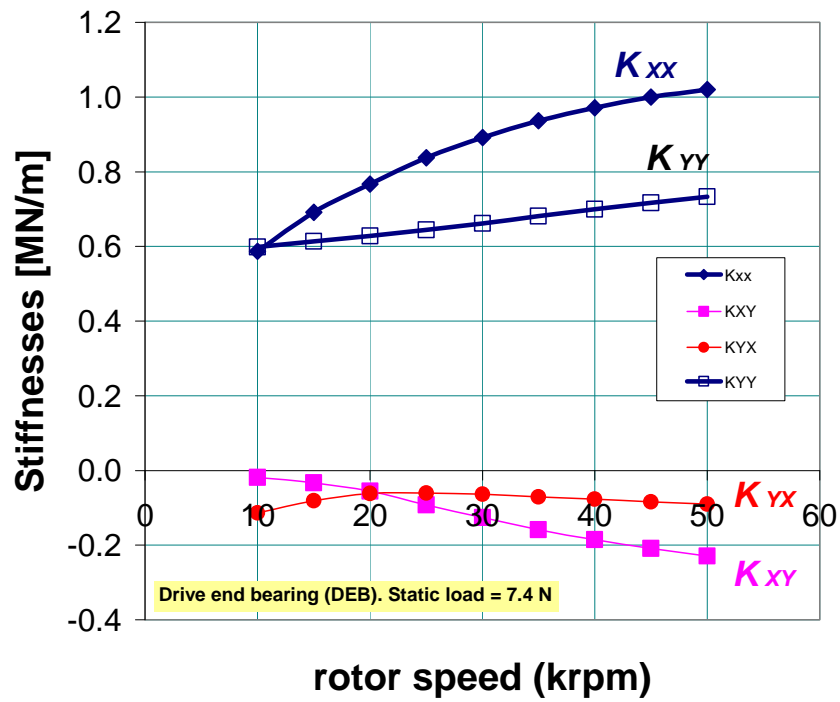


Fig B.2 Predicted synchronous speed stiffness and damping coefficients for metal mesh bearing on rotor drive end (DEB). Static load = 7.4 N